



## New perspectives on lateritic weathering process over karst area – Geochemistry and Si-Li isotopic evidence

Hongbing Ji<sup>a,\*</sup>, Cheng Chang<sup>a</sup>, Howard Omar Beckford<sup>a</sup>, Changshun Song<sup>b</sup>, Ruth E. Blake<sup>c</sup>

<sup>a</sup> School of Energy and Environmental Engineering, University of Science and Technology Beijing, Beijing 100083, China

<sup>b</sup> State Key Laboratory of Environmental Geochemistry, Institute of Geochemistry, Chinese Academy of Sciences, Guiyang 550002, China

<sup>c</sup> Department of Geology and Geophysics, Yale University, New Haven, CT 06511, United States

### ARTICLE INFO

#### Keywords:

Li isotopes  
Si isotopes  
Chemical weathering  
Terra rossa

### ABSTRACT

Silicon and lithium isotopes are increasingly used to trace current and past weathering processes. Herein, four soil profiles (SL1, SL2, XNC, and DP) in the karst critical zone in southwest China were studied. The bedrock of the SL1, SL2, and XNC profiles are limestone, while the bedrock of the DP profile is shale. By analyzing their major elements, trace elements, and mineral compositions as well as using Si and Li isotope methods, we were able to identify the material source of the laterite in southwest China and study its element behavior and isotope fractionation characteristics during the weathering process. The results show that the  $\delta^{30}\text{Si}$  of the profiles overlying limestone (SL1, SL2, and XNC) range from  $-0.5\text{‰}$  to  $0.7\text{‰}$ , and those of the  $\delta^7\text{Li}$  range from  $0.28\text{‰}$  to  $3.54\text{‰}$ , while the profile overlying shale (DP) has a large range of  $\delta^{30}\text{Si}$  variation (from  $-1.2\text{‰}$  to  $1.1\text{‰}$ ). The results reveal a clear inheritance from the underlying bedrock, indicating that the profiles reflect in-situ weathering. Although no obvious relationship exists among the chemical index of alteration (CIA), the  $\delta^{30}\text{Si}$ , and the  $\delta^7\text{Li}$ , a significant correlation between  $\delta^{30}\text{Si}$  and  $\delta^7\text{Li}$  indicates that the isotope fractionation of the studied profiles is mainly affected by the dissolution and formation of minerals during the weathering process, and the biological effect is relatively small. Further, a diagram of Li/Al versus  $\delta^7\text{Li}$  shows a decrease in both Li/Al and  $\delta^7\text{Li}$  during weathering.

### 1. Introduction

A critical zone in a soil–plant–water system may be defined as a system occupying the space from the upper limit of vegetation to the lower limit of groundwater (Brantley et al., 2007). This zone is also known as a near-surface system, and controls the conversion of elements on the Earth's surface (Anderson et al., 2004). The study of chemical weathering, soil formation, and the origin of the overlying red soil in karst areas is essential to understand the complex interactions among the processes involved in the functioning and shaping of critical zones (Mee et al., 2004).

Terra rossa is a weathering product of bedrock under tropical and subtropical climate conditions. It is widely distributed in the karst critical zone of the Yunnan Guizhou Plateau (Bates and Jackson, 1987; Durn et al., 1999). Although some studies have been carried out on red soil in southern China, the understanding of the migration and distribution of elements as well as the formation and evolution of soil during weathering remains limited. Many uncertain possibilities exist for the origin

and resources of terra rossa. Some possible sources include: (1) insoluble residues of carbonate and rubification that occur during weathering (Ji et al., 2004a; Whitehead et al., 1993); (2) accumulation of clastic rock in bedrock (Cooke et al., 2007; Driese et al., 2003); (3) allochthonous weathering materials from adjacent uplands or distant non-carbonate rocks (e.g., volcanic ash and Chinese loess) (Jackson, 1982; Muhs and Budahn, 2009). Ji et al. (2004a) concluded that underlying carbonatite is the parent material of terra rossa in the Guizhou province, depicting a possible two-stage evolution model of the red residue developed on carbonate rocks using mineralogical and geochemical data. However, other researchers (Nihlen and Olsson, 1995; Yaalon, 1997) concluded that significant additions of eolian material formed terra rossa in some regions. Thus, the origin of terra rossa and its relationship to its underlying carbonates require further research (Feng et al., 2009).

Previous studies have employed soil physicochemical parameters, particle size, mineralogical, element behavior, and other traditional geochemical methods to analyze terra rossa in critical zones (Blackburn, 1983; Yalcin and Ilhan, 2008). Of these, different isotopic composition

\* Corresponding author at: University of Science and Technology Beijing, Xueyuan Road No. 30, Haidian District, Beijing 100083, China.

E-mail address: [ji.hongbing@hotmail.com](mailto:ji.hongbing@hotmail.com) (H. Ji).

<https://doi.org/10.1016/j.catena.2020.105022>

Received 11 February 2020; Received in revised form 28 October 2020; Accepted 30 October 2020

Available online 10 November 2020

0341-8162/© 2020 Elsevier B.V. All rights reserved.

research has contributed largely to the current understanding of terra rossa. Sr and Nd isotopes have been used as indicators of soil parent material while Fe has been used to characterize different supergene geochemical cycling processes and ore deposit formation/evolution (Capo et al., 1998; Dauphas et al., 2017; Kennedy et al., 1998). Silicon isotopes ( $^{28}\text{Si}$ ,  $^{29}\text{Si}$ , and  $^{30}\text{Si}$ ) are commonly used as weathering tracers in weathering to understand complex biogeochemical processes occurring in critical zones. (Ding et al., 2004; Georg et al., 2006; Opfergelt and Delmelle, 2012; Opfergelt et al., 2008; Ziegler et al., 2005a). Lithium isotopes have been considered for use as a potential tool to trace soil sources, research soil evolution, and determine recent weathering degrees (Pistiner and Henderson, 2003; Rudnick et al., 2004; Vigier et al., 2008). Due to the large quality difference between the two Li isotopes ( $^6\text{Li}$  and  $^7\text{Li}$ ), Li is hardly affected by lithology during weathering (Tsai et al., 2014). Further, as Si and Li have only one valence state, they are not affected by redox environments. During the weathering process, heavy isotopes  $^{30}\text{Si}$  and  $^7\text{Li}$  prefer to enter a dissolved phase, while light isotopes exist in the residue (Kisakurek et al., 2004; Zack et al., 2003). However, biological processes can cause the fractionation of Si isotopes, while they have no apparent impact on Li isotopes (Millot et al., 2010).

Therefore, a combined study of Si and Li isotope systematics can potentially yield contrasting but complementary information regarding carbonate rock weathering and the origin of terra rossa.

In low-temperature environments on the Earth's surface,  $^{28}\text{Si}$  often combines with newly formed clay minerals and other solid phase materials, resulting in the enrichment of heavy isotopes in residual solutions (Opfergelt and Delmelle, 2012; Yang and Zhang, 2019; Ziegler et al., 2005a, 2005b). This variable fractionation is the result of weathering conditions. However, Si isotopes are fractionated by biological processes, wherein light isotopes are preferentially taken by organisms, such as plant-forming phytoliths and diatoms (Alexandre et al., 1997; Cornelis et al., 2010; La Rocha, 2002). Consequently, biological and chemical weathering processes can cause serious fractionation of Si isotopes. Previous studies have suggested that secondary mineral formation and Li adsorption are the two major processes controlling the isotopic fractionation of Li during weathering. Although different minerals tend to have variable fractionation factors, in general, light isotopes of  $^6\text{Li}$  are preferentially incorporated into the solid phase (Bouman et al., 2004; Dellinger et al., 2014). Li isotopes are not affected by biological processes, and the dissolution of rocks is thought to cause

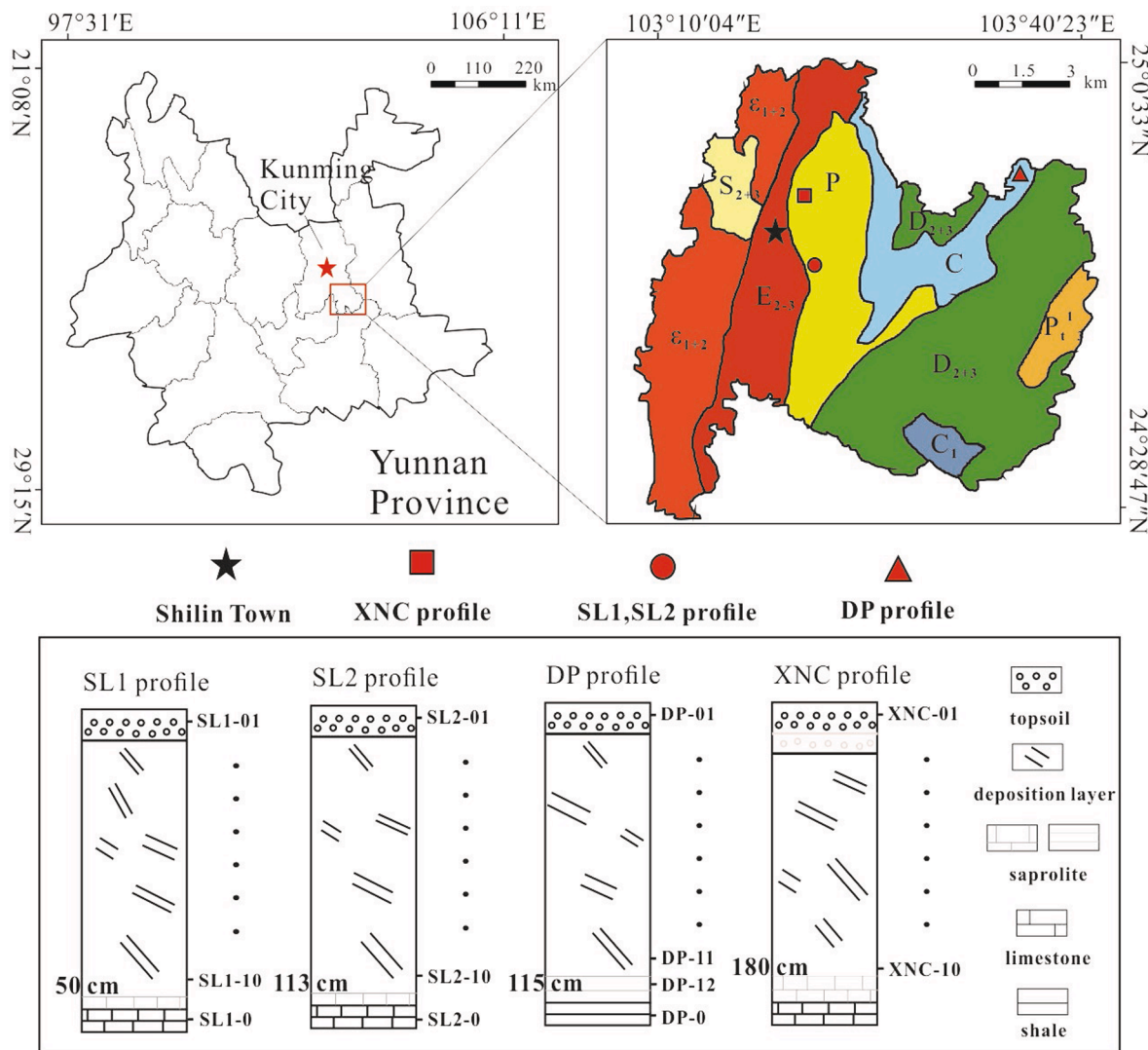


**Fig. 1.** (a) Location diagrammatic sketch showing study area (b) Sampling location in Shilin county, Yunnan province, Southwest China and (c) Schematic representation of studied weathering profiles.  $C_1$ , Limestone intercalated with Dolomite of Lower Carboniferous;  $D_{2+3}$ , Limestone and Sandstone Shale Intercalated with Dolomite of Middle-Upper Devonian series;  $P_1$ , Slate, Phyllite, Siltstone intercalated with Limestone of Sinian period;  $\epsilon_{1+2}$ , Limestone and Dolomite of Middle-Lower Cambrian;  $S_{2+3}$ , Limestone and Dolomite of Middle-Upper Silurian;  $P$ , Limestone of Permian period;  $C$ , Limestone intercalated with Dolomite of Carboniferous period;  $E_{2-3}$ , Sandstone and Mudstone intercalated with Marl of Paleogene period.

negligible isotope fractionation. During soil formation (pedogenesis), Li may be released from primary minerals and incorporated into secondary minerals (clays). The degree of isotopic fractionation also depends on the mineralogical characteristics of the clay minerals formed during weathering (Millot et al., 2010; Ushikubo et al., 2008).

In this study, we selected four typical red soil profiles in the karst critical zone and combined Li and Si isotopes with similar geochemical and mineralogical characteristics to trace the chemical weathering process of karst critical zones in the Yunnan Guizhou Plateau in order to evaluate the characteristics of terra rossa more scientifically and systematically. Our results provide new geochemical evidence for the origin of terra rossa.

## 2. Materials and methods

### 2.1. Study area

The study area is located in the Shilin Karst District of Shilin Yi Autonomous County, Kunming. It is approximately 86 km from the town center of Kunming in Yunnan, China. The GPS coordinates of the area and sampling profiles are between 24°30' – 25°03' N and 103°10' – 103°40' E (Fig. 1). The topography of the area includes stone forests, low mountains, highland hills, peaks, karst caves, and lakes. The parent bedrock materials mainly include carbonate rocks, sandstone, shale, mudstone, and basalt. The main soil type in the area is terra rossa. The study area has a subtropical plateau climate, wherein the region experiences warm and humid conditions from May to October and cold and dry conditions from November to April. The summer and fall are rainy seasons, while the winter and spring are dry seasons. The mean annual temperature is 16.3 °C and the mean annual precipitation is 800–850 mm.

### 2.2. Soil profile and sampling

The shilin 1 (samples SL1-10, elevation: 1770 m, location: 24°48'56" N, 103°18'56" E) and Shilin 2 profiles (samples SL2-10, elevation: 1730 m, location: 24°48'56" N, 103°18'53" E) (Figs. 1, S1, and S2) are located in the undeveloped wild shilin area near the Stone Forest scenic area. The SL2 sampling point is on the hillside steep slope below SL1. The coverage vegetation of the profile is low shrub. The Xinacun profile (samples XNC1-11, elevation: 1720 m, location: 24°49'6" N, 103°18'37" E) is located on a mountain slope around a construction site on the

upland landscape (Figs. 1 and S3). It is a vertical soil profile recently established by an excavator. The Dapo profile (samples DP1-12, elevation: 1920 m, location: 24°50'21" N, 103°23'26" E) is in the lower gully region of an upland landscape (Figs. 1 and S4). Note that the SL1, SL2, and XNC profiles are developed on limestone and the DP profile is developed on shale. The sampling depth and soil classification are listed in Table 1. The area comprises a large amount of thatched grass, few shrubs, and a small number of coniferous pine trees. For soil sample collection, the surface soil was removed, and fresh samples were collected from the bottom to top of the profile.

### 2.3. Soil preparation and analysis

A total of 43 soil samples from the four profiles were collected. Soil samples were air-dried and impurities such as plant roots, debris, and gravel were removed. The soil samples were placed in sealed polyethylene bags for preservation, pretreatment, and analysis. The pH, total organic carbon (TOC), soil density, concentrations of major, trace, and rare earth elements (REEs), and the isotopic composition of Li and Si were determined. Soil pH values were determined by the "China agricultural standard – soil pH determination" (NY-T 1377-2007). The total soil density was determined according to "NF X31-510-1993" soil quality and the paraffin coating method. The carbon contents of the soil samples were determined using a TOC analyzer (Liquid SOC II). The powder soil samples were pretreated with 1 mol/L HCl, and carbonate minerals were removed.

The mineral composition was determined using a Dmax/2200 model X-ray diffractometer, with the instrument standard Cu K $\alpha$  target, and settings of 40 kV, 20 mA, and scanning scope for 2–60°.

Major and trace elements were determined at the Beijing Institute of Geology, Nuclear Industry. The major elements, Al<sub>2</sub>O<sub>3</sub>, SiO<sub>2</sub>, Fe<sub>2</sub>O<sub>3</sub>, and TiO<sub>2</sub>, were determined via X-ray fluorescence spectrometry (XRF) (Philips PW2404 X-ray fluorescence spectrometer) in accordance with the GB/T14506.28-2010 silicate rock chemical analytical procedure. The trace elements Li, Th, U, Nb, Ta, and REE contents of each sample was analyzed using high-resolution inductively coupled plasma mass spectrometry (HR-ICP-MS) (Element I, Finnigan MAT Company) according to the DZ/T0223-2001 ICP-MS procedure at a temperature of 20 °C and a humidity of 30%. The loss-in-ignition (LOI) was also provided by the Beijing Institute of Geology, Nuclear Industry.

Approximately 0.010 g of each air-dried soil sample was accurately weighed with a 400 mesh sieve and placed into a 25 mL fluoroethylene

**Table 1**  
Soil classification of study profiles.

Sample	Depth(cm)	sand	silt	clay	Soil texture	Sample	Depth(cm)	sand	silt	clay	Soil texture
SL1-1	5	44.16	47.82	8.02	Silty loam	SL2-1	5	52.04	41.28	6.68	Loam
SL1-2	10	28.52	60.32	11.16	Silty loam	SL2-2	17	43.87	47.13	9	Loam
SL1-3	15	29.52	58.11	12.37	Silty loam	SL2-3	29	35.85	55.89	8.26	Silty loam
SL1-4	20	22.23	63.92	13.85	Silty loam	SL2-4	41	32.87	59.37	7.76	Silty loam
SL1-5	25	28.2	55.92	15.88	Silty clay loam	SL2-5	53	48.71	40.38	10.91	Loam
SL1-6	30	27.11	55.98	16.91	Silty clay loam	SL2-6	65	30.22	59.13	10.65	Silty loam
SL1-7	35	21.29	59.05	19.66	Silty clay loam	SL2-7	77	44.57	46.33	9.1	Loam
SL1-8	40	22.69	60.24	17.07	Silty clay loam	SL2-8	89	38.95	51.33	9.72	Silty loam
SL1-9	45	23.58	63.67	12.75	Silty loam	SL2-9	101	51.81	40.41	7.78	Loam
SL1-10	50	19.06	64.27	16.67	Silty clay loam	SL2-10	113	35.22	57.19	7.59	Silty loam
XNC-1	5	50.4	42.36	7.24	Loam	DP-1	5	6.73	53.77	39.5	Sandy clay
XNC-2	15	51.21	41.44	7.35	Loam	DP-2	15	6.62	56.66	36.72	Sandy clay
XNC-3	25	42.95	48.91	8.14	Loam	DP-3	25	1.88	57.19	40.93	Sandy clay
XNC-4	35	46.91	44.93	8.16	Loam	DP-4	35	1.03	57.72	41.25	Sandy clay
XNC-5	45	48.33	43.76	7.91	Loam	DP-5	45	0.8	58.62	40.58	Sandy clay
XNC-6	55	39.48	51.8	8.72	Silty loam	DP-6	55	1.4	56.84	41.76	Sandy clay
XNC-7	75	36.03	55.3	8.67	Silty loam	DP-7	65	0	49.37	50.63	Clay
XNC-8	95	42.26	48.14	9.6	Loam	DP-8	75	6.2	62.03	31.77	Sandy clay
XNC-9	135	45.09	47.11	7.8	Loam	DP-9	85	1.61	61.79	36.6	Sandy clay
XNC-10	185	46.09	44.71	9.2	Loam	DP-10	95	10.26	63.46	26.28	Sandy clay
XNC-11	245	41.77	54.11	4.12	Loam	DP-11	105	4.52	67.25	28.23	Sandy clay
						DP-12	115	4.3	65.3	25.3	Sandy clay

**Table 2**

Lithium concentrations ( $\mu\text{g/g}$ ), isotopic compositions, and major (wt.%) and trace elements ( $\mu\text{g/g}$ ) data for profiles in Yunnan Plateau, Southwestern China. Major and loss on ignition (LOI) values are in weight percent (wt %) and trace elements values are in ( $\mu\text{g/g}$ ). The chemical index of alteration (CIA) =  $\text{Al}_2\text{O}_3/(\text{Al}_2\text{O}_3 + \text{CaO} + \text{Na}_2\text{O} + \text{MnO})$ , (Nesbitt and Young, 1982).

Sample	Depth cm	pH	density g/cm <sup>3</sup>	TOC g/kg	TN g/kg	LOI	CIA	$\delta^{30}\text{Si}$	$\delta^7\text{Li}$	SiO <sub>2</sub> %	Al <sub>2</sub> O <sub>3</sub> %	Fe <sub>2</sub> O <sub>3</sub> %	FeO %	TiO <sub>2</sub> %	Li ppm	Th ppm	U ppm	Nb ppm	Ta ppm
SL1-1	5	5.99	1.14	0.286	0.05	20.45	86.63	-0.3	-0.08	43.87	21.31	9.66	2.78	0.92	55.4	17.9	3.06	16.5	1.24
SL1-2	10	6.025	1.83	2.255	0.168	21.12	86.05	0	-0.28	42.48	21.14	10.04	2.53	0.92	57.9	17.9	3.05	16.5	1.22
SL1-3	15	6.09	1.75	2.051	0.154	19.63	86.75	-0.3	1.19	43.47	21.73	10.08	1.94	0.939	61.3	18.3	3.18	17.3	1.29
SL1-4	20	6.075	1.89	1.676	0.142	19.4	86.72	-0.4	2.29	44.02	21.49	9.95	1.23	0.933	59.8	17.7	3.1	17	1.25
SL1-5	25	6.015	1.32	1.764	0.132	18.81	86.73	-0.2	-0.09	44.74	21.48	9.9	1.23	0.94	57.9	18.2	3.04	16.9	1.24
SL1-6	30	6.02	2.01	1.56	0.122	18.63	86.62	-0.3	0.65	44.83	21.48	9.94	1.34	0.931	62.5	18.2	3.14	17.1	1.28
SL1-7	35	6.055	2.04	1.372	0.113	18.65	86.76	-0.2	0.52	44.94	21.54	9.93	1.44	0.936	63.5	18	3.03	17	1.29
SL1-8	40	6.04	1.61	1.41	0.111	17.63	86.43	-0.5	1.58	46.87	21.04	9.61	1.11	0.939	57.1	17.4	2.9	16.9	1.24
SL1-9	45	5.995	1.74	1.157	0.102	17.12	86.17	-0.3	0.44	47.23	20.63	9.9	1.07	0.948	61	17.5	3.05	17.4	1.27
SL1-10	50	5.945	1.58	0.953	0.087	16.41	85.53	-0.5	1.45	47.83	19.58	11.09	1	0.926	51.7	16.2	3.06	16.1	1.21
SL1-0	100		1.69			42.86	0.24		0.09	1.05	0.246	0.01	0.41	0.009	1.15	0.172	<0.002	0.208	0.128
SL2-1	5	5.02	1.65	2.118	0.16	9.8	83.53	0	1	72.4	9.63	5.08	1.69	1	31.1	13.2	2.61	17.7	1.34
SL2-2	17	5.065	1.16	0.729	0.072	7.78	83.95	-0.2	2.3	71.91	11.1	5.9	0.81	1.05	36.1	15.2	2.85	18.6	1.37
SL2-3	29	5.11	1.64	0.413	0.058	7.65	88.12	-0.1	0.72	71.06	12.16	6.1	0.53	1.07	38.7	17	3.2	19.4	1.45
SL2-4	41	5.22	1.76	0.351	0.051	7.03	87.78	-0.2	3.54	73.02	11.26	5.66	0.65	1.09	36.1	14.7	2.55	17.4	1.26
SL2-5	53	5.05	1.62	0.24	0.045	6.16	88.46	-0.1	3	75.36	10.43	5.31	0.33	1.09	34.6	14	2.67	19.1	1.42
SL2-6	65	5.085	1.68	0.153	0.037	5.71	88.51	0	1.97	76.96	9.95	4.78	0.36	1.11	32.9	14.5	2.68	19.7	1.49
SL2-7	77	5.445	2.30	0.154	0.032	5.4	87.99	-0.2	2.19	78.05	9.31	4.55	0.44	1.13	32.2	15.1	2.73	20.5	1.48
SL2-8	89	5.575	1.42	0.158	0.038	5.34	87.31	-0.3	2.44	78.21	9.23	4.49	0.37	1.13	33.5	14.3	2.82	20.8	1.59
SL2-9	101	5.255	2.04	0.16	0.046	5.51	87.37	-0.2	2.7	77.36	9.75	4.52	0.29	1.17	32.9	14.7	2.9	21.2	1.57
SL2-10	113	5.17	1.83	0.145	0.043	5.64	86.06	-0.1	2.08	76.23	10.22	4.84	0.32	1.16	33.2	14.5	2.73	20.6	1.56
SL2-0	163		1.71			43.14	0.11		-2.26	0.609	0.107	0.01	0.23	0.012	0.392	0.064	<0.002	0.117	0.038
XNC-1	5	5.01	1.52	0.942	0.089	8.09	78.02	-0.2	3.29	72.29	10.32	5.05	0.7	0.953	35.2	13.1	2.82	16.9	1.14
XNC-2	15	5.36	1.75	0.712	0.08	7.3	77.59	-0.1	3.42	73.63	10.01	4.79	0.61	0.958	35.5	13.4	2.9	17.5	1.22
Sample	Depth cm	pH	density g/cm <sup>3</sup>	TOC g/kg	TN g/kg	LOI	CIA	$\delta^{30}\text{Si}$	$\delta^7\text{Li}$	SiO <sub>2</sub> %	Al <sub>2</sub> O <sub>3</sub> %	Fe <sub>2</sub> O <sub>3</sub> %	FeO %	TiO <sub>2</sub> %	Li ppm	Th ppm	U ppm	Nb ppm	Ta ppm
XNC-3	25	5.44	1.59	0.799	0.081	7.84	70.59	-0.3	3.42	72.30	9.89	4.97	0.58	0.943	33.9	13.1	2.67	16.1	1.09
XNC-4	35	5.77	1.40	0.257	0.049	6.46	80.82	-0.3	3.72	73.64	10.28	5.83	0.5	1.06	34.6	13.8	3.17	18.7	1.25
XNC-5	45	5.93	1.78	0.286	0.049	7.02	72.07	0.6	1.43	73.39	9.98	5.14	0.37	1.01	33.4	13.4	3.05	18.9	1.35
XNC-6	55	6.07	1.84	0.185	0.046	6.72	80.67	0.7	2.9	71.71	10.8	6.7	0.45	1.05	33.1	14.9	3.37	19.8	1.38
XNC-7	75	6.07	1.55	0.121	0.044	7.31	79.54	0.1	2.48	69.08	12.67	5.89	0.39	0.939	33.8	14.1	3.04	17	1.25
XNC-8	95	6.055	1.94	0.154	0.047	7.8	80.91	0.1	1.76	67.64	12.91	7.06	0.43	1.03	32.9	15.1	3.35	18.7	1.34
XNC-9	135	6.075	1.91	0.189	0.103	7.37	79.60	0.1	1.29	69.05	12.97	5.41	0.43	0.906	34.7	14.2	2.86	16.6	1.24
XNC-10	185	5.63	1.91	0.118	0.047	6.66	80.04	0.2	3.14	70.66	11.9	6.01	0.34	0.923	34.2	13.8	3.03	16.8	1.19
XNC-11	245	5.54	2.11	0.058	0.038	5.67	78.49	-0.1	2.29	74.67	10.72	4.23	0.42	0.856	32.7	13.2	2.61	16.1	1.14
DP-1	5	4.285	1.29	0.919	0.089	11.85	92.02	-0.1		50.82	20.34	12.01	1.1	0.961	156	27.1	5.81	21.8	1.53
DP-2	15	4.18	1.13	0.288	0.061	10.5	92.30	0.5		53.04	21.18	9.21	0.43	0.973	172	27.6	5.3	23.5	1.64
DP-3	25	4.23	1.81	0.217	0.061	11.5	92.54	-0.3		48.96	22.31	11.09	0.47	0.956	160	26	6.42	22.5	1.57
DP-4	35	4.27	1.93	0.179	0.058	11.61	92.78	1.1		48.85	22.45	11.4	0.47	0.917	155	28.5	7.12	22.2	1.57
DP-5	45	4.16	1.95	0.189	0.056	10.33	92.55	0.3		51.4	22.37	9.6	0.57	0.965	174	28.2	5.51	22.5	1.6
DP-6	55	4.235	1.86	0.189	0.053	10.09	92.10	0.6		51.09	21.96	10.14	0.44	0.909	166	27.3	6.52	22.2	1.57
DP-7	65	4.055	1.64	0.177	0.065	12.46	93.58	-0.9		45.05	24.42	12.84	0.31	0.895	183	29.8	7.31	20.9	1.48
DP-8	75	4.26	1.64	0.184	0.063	9.81	91.62	0.3		50.56	20.85	11.87	0.33	0.88	133	25.2	6.87	21.4	1.51
DP-9	85	4.24	1.25	0.143	0.067	13.11	94.11	-1.1		44.4	25.45	12.26	0.42	0.859	164	28.2	7.48	20.5	1.42
DP-10	95	4.285	2.06	0.126	0.056	10.83	91.82	-1.2		48.22	20.85	13.71	0.49	0.829	121	22.7	7.11	19.8	1.38
DP-11	105	4.365	2.08	0.15	0.05	8.14	90.84	-1.1		59.48	17.77	8.47	0.47	0.92	118	22.5	5.07	21.6	1.45
DP-12	115	5.16	2.07	0.286	0.05	8.21	91.09	-1		59.82	19.77	5.15	0.48	0.946	158	24.6	3.86	19.3	1.39
DP-0	145		1.83			8.02	90.67			61.16	19.48	4.37	0.47	0.974	140	24.6	3.62	23.2	1.62

The chemical index of alteration (CIA) =  $\text{Al}_2\text{O}_3/(\text{Al}_2\text{O}_3 + \text{CaO} + \text{Na}_2\text{O} + \text{MnO})$ , (Nesbitt and Young, 1982)

**Table 3**  
REE concentrations of soil samples from four profiles in Yunnan Plateau, Southwestern China. All concentrations are normalized to the bulk sample and given in  $\mu\text{g/g}$ . The Ce anomaly ( $\delta\text{Ce} = \text{Ce}_N / [(\text{La}_N + \text{Pr}_N) / 2]$ ) were calculated. Listed also the  $(\text{La}/\text{Yb})_N = ((\text{La}/\text{La}_N) / (\text{Yb}/\text{Yb}_N))$ ,  $(\text{La}/\text{Sm})_N = ((\text{La}/\text{La}_N) / (\text{Sm}/\text{Sm}_N))$  and  $(\text{Gd}/\text{Yb})_N = ((\text{Gd}/\text{Gd}_N) / (\text{Yb}/\text{Yb}_N))$  ratios indicating the degree of REE.

Sample Depth(m)	SL1-1 5	SL1-2 10	SL1-3 15	SL1-4 20	SL1-5 25	SL1-6 30	SL1-7 35	SL1-8 40	SL1-9 45	SL1-10 50	SL1-0 100	SL2-1 5	SL2-2 17	SL2-3 29	SL2-4 41	SL2-5 53	SL2-6 65	SL2-7 77	SL2-8 89	SL2-9 101	SL2-10 113	SL2-0 163	XNC-1 5	XNC-2 15
La	42.4	44.3	43.5	43.5	42.7	43.8	44.7	43.4	41.7	45.1	0.617	31.9	33.6	35.5	33.3	31.3	33	35.6	34.1	38.7	37.1	4.44	34.3	35.1
Ce	85.8	83.7	78.3	83.6	88.9	84.5	85	84.1	80.2	72.6	1.07	65.6	70.7	81.9	73.6	64	68.3	64.2	61.3	67.4	60.9	0.603	61.6	70.2
Pr	11.9	12.6	12.1	11.9	12	12.3	12.6	12.2	11.6	13.1	0.147	7.15	7.62	7.82	7.39	6.73	7.22	7.36	7.27	8.21	7.63	0.636	7.56	7.84
Nd	48	51.2	49.4	47.7	49.2	50	50.1	48.3	46.6	53	0.562	26.2	27.5	28.7	26.4	24.4	25.6	26.3	25.8	28.9	26.6	2.39	27.2	28.2
Sm	11.2	11.8	11.5	11.2	11.2	11.6	11.4	11.1	10.8	12.5	0.112	4.96	5.17	5.34	5	4.37	4.54	4.48	4.57	5.02	4.52	0.316	4.71	5.21
Eu	2.46	2.59	2.49	2.49	2.48	2.58	2.5	2.41	2.41	2.77	0.021	0.92	0.914	0.905	0.897	0.794	0.776	0.729	0.768	0.774	0.76	0.065	0.871	0.896
Gd	10	10.3	10.1	9.85	10	10	10.1	9.62	9.5	10.8	0.095	4.36	4.43	4.48	4.17	3.65	3.92	3.76	3.75	3.99	3.8	0.317	4.08	4.34
Tb	1.9	2.01	1.97	1.93	1.95	1.94	1.96	1.82	1.82	2.1	0.019	0.779	0.804	0.824	0.708	0.637	0.661	0.665	0.66	0.691	0.651	0.047	0.714	0.775
Dy	10.2	10.7	10.5	10.3	10.5	10.5	10.4	9.78	9.79	11.2	0.106	4.23	4.28	4.42	3.69	3.47	3.53	3.65	3.61	3.56	3.56	0.182	3.64	3.96
Ho	2.13	2.2	2.19	2.09	2.14	2.21	2.16	2.01	2.02	2.29	0.024	0.916	0.922	0.919	0.766	0.726	0.755	0.768	0.758	0.792	0.762	0.034	0.802	0.865
Er	5.8	5.96	5.88	5.71	5.82	6	5.79	5.44	5.59	6.06	0.063	2.55	2.63	2.65	2.21	2.08	2.16	2.28	2.31	2.33	2.25	0.084	2.31	2.5
Tm	0.92	0.921	0.946	0.91	0.927	0.939	0.927	0.853	0.884	0.933	0.009	0.427	0.43	0.428	0.357	0.351	0.356	0.39	0.375	0.385	0.378	0.009	0.373	0.402
Yb	5.63	5.78	5.78	5.55	5.73	5.66	5.65	5.26	5.42	5.71	0.061	2.64	2.73	2.81	2.23	2.24	2.28	2.31	2.39	2.49	2.41	0.05	2.41	2.69
Lu	0.887	0.9	0.905	0.876	0.882	0.911	0.89	0.818	0.883	0.89	0.009	0.414	0.427	0.449	0.349	0.348	0.354	0.368	0.375	0.404	0.39	0.007	0.398	0.424
$\Sigma\text{REE}$	239.23	244.96	235.56	237.61	244.43	242.94	244.18	237.11	229.22	239.05	2.92	153.05	162.16	177.15	161.07	145.10	153.45	152.86	148.04	163.65	151.71	9.18	150.97	163.40
$\Sigma\text{LREE}$	201.76	206.19	197.29	200.39	206.48	204.78	206.30	201.51	193.31	199.07	2.53	136.73	145.50	160.17	146.59	131.59	139.44	138.67	133.81	149.00	137.51	8.45	136.24	147.45
$\Sigma\text{HREE}$	37.47	38.77	38.27	37.22	37.95	38.16	37.88	35.60	35.91	39.98	0.39	16.32	16.65	16.98	14.48	13.50	14.02	14.19	14.23	14.64	14.20	0.73	14.73	15.96
$\Sigma\text{LREE}/\Sigma\text{HREE}$	5.39	5.32	5.16	5.38	5.44	5.37	5.45	5.66	5.38	4.98	6.55	8.38	8.74	9.43	10.12	9.75	9.95	9.77	9.40	10.18	9.68	11.58	9.25	9.24
LREE%	84.34	84.17	83.75	84.34	84.47	84.29	84.49	84.99	84.33	83.27	86.76	89.34	89.73	90.41	91.01	90.69	90.87	90.72	90.39	91.05	90.64	92.05	90.24	90.24
HREE%	15.66	15.83	16.25	15.66	15.53	15.71	15.51	15.01	15.67	16.73	13.24	10.66	10.27	9.59	8.99	9.31	9.13	9.28	9.61	8.95	9.36	7.95	9.76	9.76
$\delta\text{Eu}$	0.71	0.72	0.71	0.72	0.72	0.73	0.71	0.71	0.73	0.73	0.62	0.60	0.58	0.57	0.60	0.61	0.56	0.54	0.57	0.53	0.56	0.63	0.61	0.58
$\delta\text{Ce}$	0.92	0.85	0.82	0.88	0.95	0.88	0.86	0.88	0.88	0.72	0.86	1.05	1.06	1.18	1.13	1.06	1.06	0.95	0.94	0.91	0.87	0.09	0.92	1.02
$(\text{La}/\text{Yb})_N$	5.08	5.17	5.07	5.28	5.02	5.22	5.33	5.56	5.19	5.33	6.82	8.15	8.30	8.52	10.07	9.42	9.76	10.39	9.62	10.48	10.38	59.87	9.60	8.80
$(\text{La}/\text{Sm})_N$	2.38	2.36	2.38	2.44	2.40	2.38	2.47	2.46	2.43	2.27	3.47	4.05	4.09	4.18	4.19	4.51	4.57	5.00	4.69	4.85	5.16	8.84	4.58	4.24
$(\text{Gd}/\text{Yb})_N$	1.43	1.44	1.41	1.43	1.41	1.43	1.44	1.48	1.41	1.53	1.26	1.33	1.31	1.29	1.51	1.31	1.39	1.31	1.27	1.29	1.27	5.12	1.37	1.30

Sample Depth(m)	XNC-3 25	XNC-4 35	XNC-5 45	XNC-6 55	XNC-7 75	XNC-8 95	XNC-9 135	XNC-10 185	XNC-11 245	DP-1 5	DP-2 15	DP-3 25	DP-4 35	DP-5 45	DP-6 55	DP-7 65	DP-8 75	DP-9 85	DP-10 95	DP-11 105	DP-12 115	DP-0 145	
La	35.3	33.3	31.7	34.3	35.5	36.4	38.8	37.7	44.6	69	74.2	74.6	78	71.4	73.4	81	71.8	94.5	69.7	61.8	73.3	72.3	
Ce	77	60.9	58.4	61.6	61.8	64.8	70.6	68.9	80.1	120	124	128	161	120	124	127	134	156	126	111	141	137	
Pr	7.83	6.91	6.59	7.11	7.27	7.28	8.31	8.53	10.1	16.2	16.8	17.6	18.7	16.6	17.2	19.1	16.5	20.9	16.7	15.1	19	18.6	
Nd	28.4	24.5	22.9	25.3	25.6	25.2	29.5	31.6	36.4	59.8	63.3	67.6	72.3	61.8	63.8	72.2	62.3	80.2	66.1	55.7	70.4	68.5	
Sm	5.16	4.15	3.96	4.2	4.23	4.24	5.01	5.67	6.67	11.6	12	13.2	14.4	12	12.3	14.4	12.3	15.7	13.3	10.8	13.7	13.4	
Eu	0.96	0.717	0.706	0.731	0.765	0.752	0.922	1.06	1.24	2.22	2.28	2.56	2.75	2.31	2.35	2.82	2.37	3.08	2.5	2.06	2.55	2.51	
Gd	4.69	3.45	3.28	3.61	3.56	3.54	4.41	4.71	5.59	10.4	10.7	11.6	12.8	10.6	10.9	12.5	10.7	13.7	11.4	9.52	11.3	11.1	
Tb	0.805	0.595	0.569	0.634	0.614	0.624	0.751	0.818	0.942	1.98	2.02	2.22	2.4	2	2.11	2.34	2.04	2.53	2.11	1.9	2.2	2.2	
Dy	4.1	3.13	3.12	3.48	3.44	3.45	4.18	4.48	4.98	11.1	11.1	12.1	13.1	11.1	11.5	12.6	11.1	13.2	11.2	10.3	11.8	11.9	
Ho	0.887	0.681	0.685	0.778	0.793	0.781	0.916	0.988	1.06	2.5	2.5	2.72	2.94	2.47	2.54	2.77	2.45	2.91	2.41	2.27	2.54	2.64	
Er	2.45	2.03	2.01	2.32	2.41	2.38	2.7	2.81	2.97	7	7.15	7.67	8.41	6.9	7.2	7.88	6.9	8.01	6.77	6.32	7.16	7.36	
Tm	0.401	0.355	0.343	0.394	0.396	0.4	0.46	0.465	0.489	1.12	1.15	1.17	1.31	1.08	1.14	1.21	1.08	1.24	1.04	1.02	1.13	1.16	
Yb	2.51	2.26	2.25	2.54	2.61	2.6	2.79	2.92	2.96	6.73	7.08	7.18	7.84	6.78	6.94	7.39	6.65	7.56	6.29	6.32	7.27	7.37	
Lu	0.418	0.373	0.359	0.411	0.411	0.426	0.442	0.458	0.472	1.07	1.13	1.14	1.24	1.09	1.11	1.19	1.07	1.18	1.02	1.01	1.16	1.16	
$\Sigma\text{REE}$	170.91	143.35	136.87	147.41	149.40	152.87	169.79	171.11	198.57	320.72	335.41	349.36	397.19	326.13	336.49	364.40	341.26	420.71	336.54	295.12	364.51	357.20	
$\Sigma\text{LREE}$	154.65	130.48	124.26	133.24	135.17	138.67	153.14	153.46	179.11	278.82	292.58	303.56	347.15	284.11	293.05	316.52	299.27	370.38	294.30	256.46	319.95	312.31	
$\Sigma\text{HREE}$	16.26	12.87	12.62	14.17	14.23	14.20	16.65	17.65	19.46	41.90	42.83	45.80	50.04	42.02	43.44	47.88	41.99	50.33	42.24	38.66	44.56	44.89	
$\Sigma\text{LREE}/\Sigma\text{HREE}$	9.51	10.13	9.85	9.41	9.50	9.76	9.20	8.70	9.20	6.65	6.83	6.63	6.94	6.76	6.75	6.61	7.13	7.36	6.97	6.63	7.18	6.96	
LREE%	90.49	0.91	0.91	0.90	0.90	0.91	0.90	0.90	0.90	0.87	0.87	0.87	0.87	0.87	0.87	0.87	0.88	0.88	0.87	0.87	0.88	0.87	0.87
HREE%	9.51	0.09	0.09	0.10	0.10	0.09	0.10	0.10	0.10	0.13	0.13	0.13	0.13	0.13	0.13	0.13	0.12	0.12	0.13	0.13	0.12	0.13	0.13
$\delta\text{Eu}$	0.60	0.58	0.60	0.57	0.60	0.59	0.60	0.63	0.62	0.62	0.62	0.63	0.62	0.63	0.62	0.64	0.63	0.64	0.62	0.62	0.63	0.63	0.63
$\delta\text{Ce}$	1.11	0.97	0.97	0.95	0.93	0.96	0.95	0.92	0.91	0.86	0.85	0.85	1.01	0.84	0.84	0.78	0.94	0.84	0.89	0.87	0.91	0.90	
$(\text{La}/\text{Yb})_N$	9.48	9.93	9.50	9.10	9.17	9.44	9.38	8.70	10.16	6.91	7.07	7.00	6.71	7.10	7.13	7.39	7.28	8.43	7.47	6.59	6.80	6.61	
$(\text{La}/\text{Sm})_N$	4.30	5.05	5.04	5.14	5.28	5.40	4.87	4.18	4.21	3.74	3.89	3.55	3.41	3.74	3.75	3.54	3.67	3.79	3.30	3.60	3.37	3.39	
$(\text{Gd}/\text{Yb})_N$	1.51	1.23	1.18	1.15	1.10	1.10	1.28																

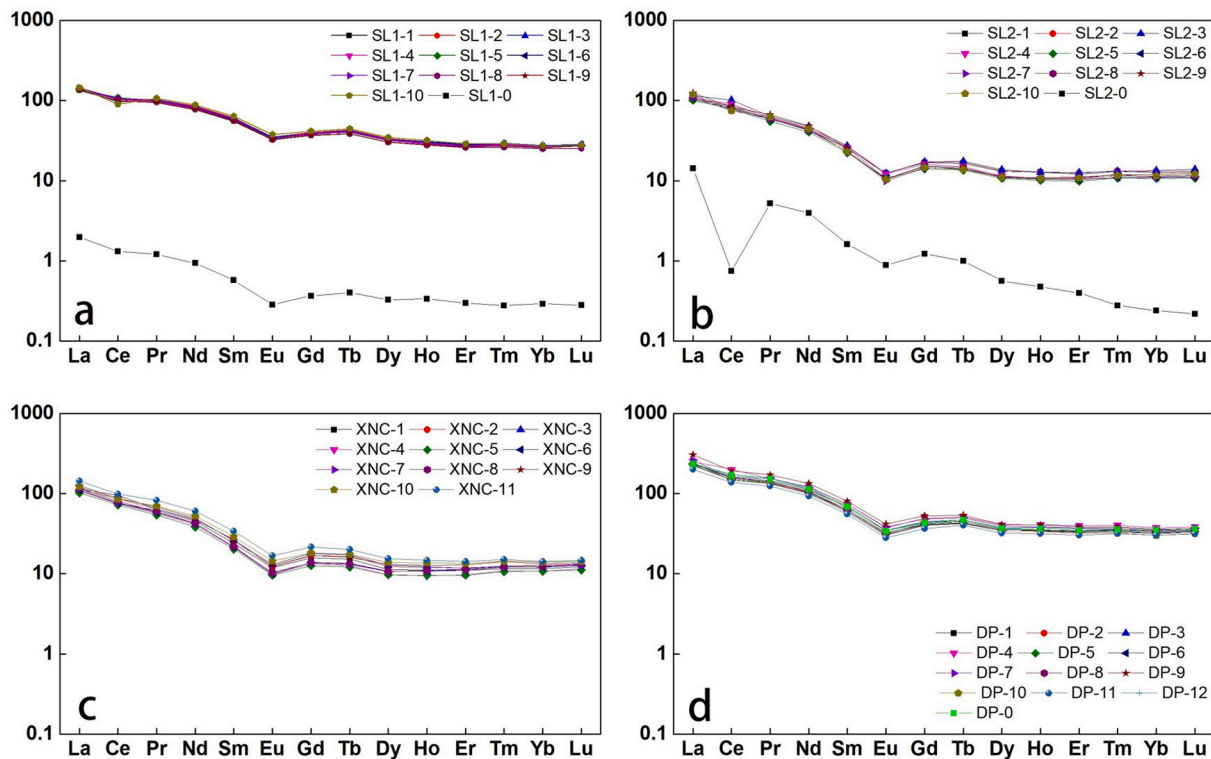


Fig. 2. Chondrite-normalized REE patterns for the studied soil profiles in Yunnan Plateau, Southwestern China. The chondrite elemental content data is from Taylor and McLennan's (1985).

digestion tank. Then, 4 mL of 15 mol/L HNO<sub>3</sub> solution was added to the tank. Next, it was sealed and placed on a 120 °C electric heating plate overnight. The cover on the electric heating plate was opened to dry the next day. This step was conducted three times, and the sample was added with 2 mL of 0.5 mol/L HNO<sub>3</sub>, 2 mL of 15 mol/L HNO<sub>3</sub>, and 3 mL of 12 mol/L HCl solutions, respectively. The sample was then added to 2 mL of 0.5 mol/L HNO<sub>3</sub> and placed on a 100 °C electric heating plate.

After digestion, Li cations were isolated through column separation to reduce sodium analysis matrix effects. The samples were loaded onto an AG50W-X12 mesh resin column. The samples were cleaned with 6 mol/L HNO<sub>3</sub> (8 mL) four times, and the resin column was cleaned with 8 mL of ultrapure water followed by a 0.5 mol/L HNO<sub>3</sub> cleaning solution (4 mL) three times. After adjusting the resin column to the concentration of eluent, 2 mL of the sample was introduced into the resin column for elution. An HNO<sub>3</sub> solution (0.5 mol/L) was used as the eluent, and an eluent within 20–48 mL was collected for analysis. The recovery rate of Li was close to 100%, thereby avoiding Li isotope fractionation during the separation process, and the Li/Na < 1 in the separated Li solution can successfully avoid matrix influence on the determination of the Li isotopes.

In this experiment, Li isotopic determination was conducted in the State Key Laboratory of Loess and Quaternary Geology with an MC-ICP-MS instrument produced by the Thermo Fisher Scientific TM company (USA). The instrument quality identification produced by plasma source mass spectrometry is wide ranging. Therefore, the standard-sample bracketing (SSB) technique was used to correct the mass fractionation in the plasma source. The reference material used was a L-SVEC standard sample provided by National Institute of Standards and Technology (NIST). The overall reproducibility and accuracy of this method was tested by repeating measurements of the andesite AGV-2 ( $\delta^7\text{Li} = +6.83 \pm 0.75\text{‰}$ ,  $\pm 2\sigma$ ,  $n = 5$ , quintic dissolution sample) and basalt reference materials BHVO-2 ( $\delta^7\text{Li} = +4.34 \pm 0.33\text{‰}$ ,  $\pm 2\sigma$ ,  $n = 5$ , quintic dissolution sample). The internal and external accuracies of this method are higher than 0.30‰ and 0.75‰, respectively.

Soil and rock samples were melted in a covered platinum crucible at

1000 °C by alkaline melting (Libo<sub>2</sub>) and dissolved in 10% nitric acid (Abraham et al., 2008). Si was then purified using triethylamine molybdate coprecipitation and burned in a covered platinum crucible at 1000 °C. Si isotope analysis was performed using the SiF<sub>4</sub> method. SiO<sub>2</sub> was placed in an Ni reactor with a metal vacuum line and reacted with BrF<sub>5</sub> at approximately 500 °C to form SiF<sub>4</sub>. The prepared SiF<sub>4</sub> was then separated at low temperatures of dry ice acetone and liquid nitrogen to remove O<sub>2</sub>, N<sub>2</sub>, BrF<sub>5</sub>, and BrF<sub>3</sub>. The trace active fluorine compounds in the SiF<sub>4</sub> were removed by a copper tube containing pure zinc particles at 60 °C. The purified SiF<sub>4</sub> was collected for Si isotope determination. Si isotopic measurements were performed with a Finnigan MAT 253 mass spectrometer, which has a total analytical accuracy greater than  $\pm 0.1\text{‰}$ , at the Key Laboratory on Isotope Geology, Ministry of Land and Resources.

### 3. Results

The compositions of the major, trace, and rare elements as well as the soil properties, including soil depth, pH, density, TOC, total nitrogen (TN), and isotopic composition of Li and Si in the soil profiles at Yunnan Plateau, southwestern China are listed in Table 2.

#### 3.1. Profile characteristics and mineral compositions

As summarized in Table 2 and Fig. S5, the soil samples from the SL1, SL2, XNC, and DP profiles are acidic, with pH ranges from 4.05 to 6.09, of which the DP profile has the highest acidity. Notably, the TOC content generally tends to decrease with depth for each profile.

Based on the international soil texture classification standard, the grain sizes of the four profiles were mainly silt, with a volume fraction nearly greater than 50%. These results indicate that all the soil profiles had obvious inheritance with different distribution characteristics (Fig. S6). The SL1, SL2, and XNC soil profiles were mainly sand and silt, while the DP soil profile was mainly silt and clay (Fig. S6).

From the XRD analysis, the SL1 profile was found to be mainly

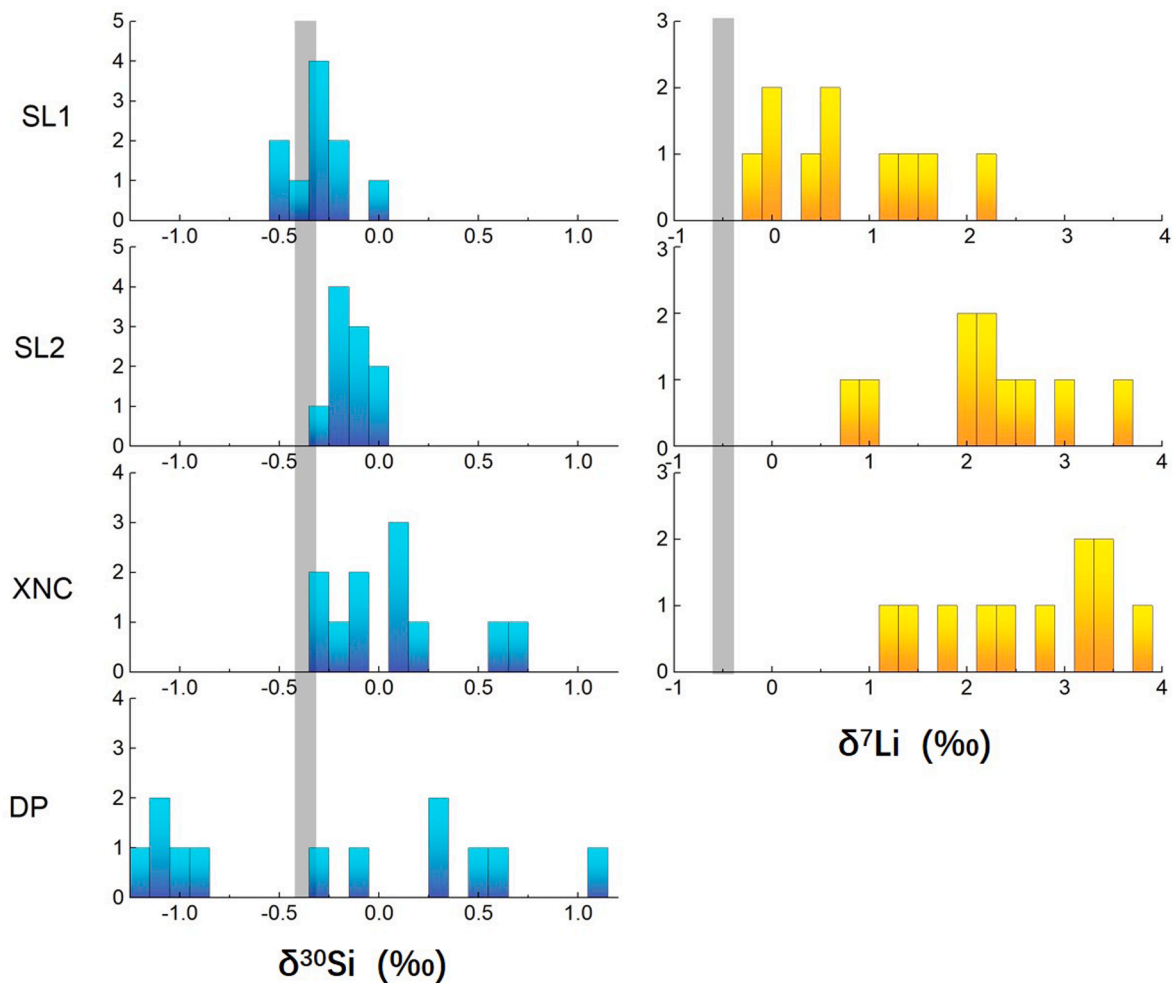


Fig. 3. The Frequency distribution of  $\delta^{30}\text{Si}$  and  $\delta^7\text{Li}$  isotopic composition in four studied soil profiles in Yunnan Plateau, Southwestern China. The shaded bar indicates the  $\delta^{30}\text{Si}$  and  $\delta^7\text{Li}$  value from Post-Archaean Australian shales (Savage et al, 2013).

composed of quartz, illite, montmorillonite, and kaolinite as well as gibbsite, goethite, hematite, anatase, and pyrrhotite (Fig. S1). Meanwhile, the SL2 and XNC soil profiles contain quartz, kaolinite, goethite, hematite, and anatase (Figs. S2 and S3). The DP soil profile consists primarily of quartz and montmorillonite, as well as some kaolinite, gibbsite, goethite, hematite, and anatase (Fig. S4). Thus, the XRD results show that the main mineral components of the four profiles are quartz and clay minerals (illite, montmorillonite, and kaolinite). However, iron-bearing minerals (magnetite and hematite) also exist. Gibbsite was found in all profiles, indicating that the profiles have experienced strong weathering. There was no obvious change in mineral composition from bottom to top in the profiles. The mineralogical composition confirms that the study profiles are mainly composed of quartz and clay minerals. Further, the soil profiles showed distinct soil layers, including an uppermost layer (top is tillage layer), regolith layer, weathered bedrock horizon, and fresh bedrock horizon.

### 3.2. Chemical composition

The chemical compositions of the profile samples are listed in Table 2. Note that the major elements vary with depth. The chemical indices of alteration (CIA) of the XNC, SL1, SL2, and DP profiles were 78, 86, 87, and 92, respectively. Meanwhile, the LOI varies among the studied profiles, wherein the SL1 profile had the highest LOI (18.78–1.57 wt%), followed by the DP profile (10.70–0.48 wt%). Finally, the SL2 and XNC profiles had the lowest LOIs (6.60–7.11 wt%

and 0.48–0.58 wt%, respectively).

REE content varied little in the study profiles, wherein the DP profile had the highest REE content, with a range of 229.22–420.71  $\mu\text{g/g}$ , while the SL1 profile had a range of 229.22–244.96  $\mu\text{g/g}$  (Table 3). The REE contents of the SL2 and XNC profiles were similar at 145.10–177.15  $\mu\text{g/g}$  and 136.87–198.57  $\mu\text{g/g}$ , respectively. Although the SL2 and XNC profiles have low REE content, they have higher light rare earth element (LREE) and heavy rare earth element (HREE) fractionation degrees [(La/Yb)<sub>N</sub> = 8.15–10.48 and 8.70–9.60]. Further, the ratio of LREE/HREE revealed a high enrichment of LREEs relative to that of HREEs (8.38–11.58 and 8.70–10.14, respectively). The LREE/HREE values of the DP and SL1 profiles ranged from 6.63 to 7.36, and from 4.98 to 6.55, respectively. Herein, the REE patterns indicate that all the study profiles have weak Ce-anomalies. The Ce-anomalies of the SL1 and DP profiles are 0.72–0.95 and 0.78–0.94, respectively (with the exception of DP-04 = 1.05), while the upper parts of the SL2 and XNC profiles have a positive Ce-anomaly, and the lower parts have a negative Ce-anomaly (0.87–1.18 and 0.91–1.12). From the base of bedrock to the top of each profile, the REE distribution patterns of the soil samples show similar and consistent characteristics. The REE patterns of the limestone samples from the bedrocks in the SL1 and SL2 profiles show distribution patterns that are consistent with those of the carbonate soil profile samples, with the exception of a sample point in SL2, thereby showing a remarkable negative Ce anomaly (Ce/Ce\* = 0.086). However, the distribution of REEs in the DP profile is not significantly different from that of the bedrock and saprolite, indicating that the DP profile (silicate)

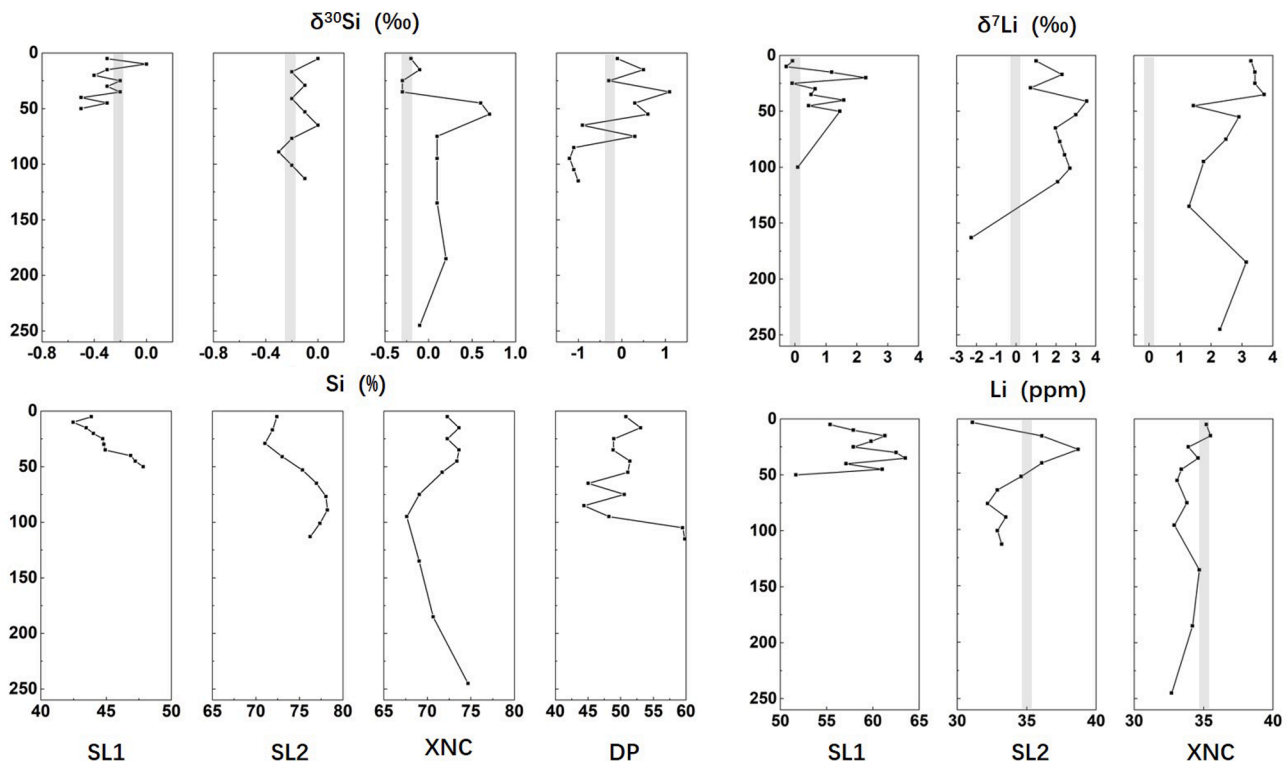


**Fig. 4.** The distribution of (a)  $\text{Al}_2\text{O}_3$  vs.  $\text{Fe}_2\text{O}_3$ , (b)  $\text{Al}_2\text{O}_3$  vs.  $\text{TiO}_2$ , (c)  $\text{SiO}_2$  vs.  $\text{Fe}_2\text{O}_3$  and (d)  $\text{SiO}_2$  vs.  $\text{Al}_2\text{O}_3$  for studied soil profiles in Yunnan Plateau, Southwestern China. In (a) and (b) the ratios in SL1 and SL2 and XNC profile are projected from the bedrock indicate bedrock dissolution. The small plots in (c) and (d) showing the  $\text{SiO}_2/\text{Fe}_2\text{O}_3$  and  $\text{SiO}_2/\text{Al}_2\text{O}_3$  ratios of SL1 and SL2 bed rock. The ratio of SL2 and XNC is always together, while the DP profile shows a significant difference. The blue arrow indicates the weathering trend of DP. Although the ratio of SL1 is different from SL2 and XNC, it also shows the same trend.

have different weathering regime with other profiles (carbonate) (Fig. 2).

### 3.3. Isotopic composition

A small range of Si isotopic composition ( $-0.5\text{‰}$  to  $1.1\text{‰}$ ) was observed in the soil samples of each profile (Table 2). The SL1 and SL2 profiles indicate a relatively small isotopic composition range ( $-0.5\text{‰}$  to  $0\text{‰}$ ; avg.  $0.5\text{‰}$ ), and fractionation ( $-0.3\text{‰}$  to  $0\text{‰}$ ; avg.  $0.3\text{‰}$ ), whereas the XNC and DP profiles show large isotopic composition ranges ( $-0.3\text{‰}$  to  $0.7\text{‰}$ ; avg.  $1\text{‰}$ ) and fractionation ( $-0.9$  to  $1.1\text{‰}$ ; avg.  $2\text{‰}$ ). The silicon isotopes in the SL1, SL2, and XNC profiles are concentrated around  $-0.3$ ,  $-0.2$ , and  $0.0\text{‰}$ , respectively. Further, the  $\delta^{30}\text{Si}$  isotopic composition showed a slightly heavy isotope shift in the SL1, SL2, and XNC profiles with landform (Fig. 3). Conversely, the silicon isotopic composition of the DP profile is scattered and appears to have both the highest and lowest values.

Overall, the  $\delta^7\text{Li}$  isotopic composition varied between  $-0.28$  and  $3.54\text{‰}$  (Table 2). For the SL1, SL2, and XNC profiles, the  $\delta^7\text{Li}$  isotopic compositions ranged from  $-0.28\text{‰}$  to  $2.29\text{‰}$  (avg.  $0.76\text{‰}$ ), from  $0.72\text{‰}$  to  $3.54\text{‰}$  (avg.  $1.78\text{‰}$ ), and from  $1.29\text{‰}$  to  $3.72\text{‰}$  (avg.  $2.64\text{‰}$ ), respectively. The Li isotope distribution range was larger than the Si isotope distribution. Similarly, however, it demonstrated a slight shift towards the heavier isotope for the SL1, SL2, and XNC profiles with changing landform (Fig. 3).

## 4. Discussion

### 4.1. Provenance tracing of terra rossa in the Shilin profiles

#### 4.1.1. Traditional geochemical methods

During chemical weathering, Al, Ti, and Fe are less mobile than other elements (Braun et al., 1993; Ji et al., 2004a; Tsai et al., 2007) and have

distinct characteristics and geochemical behavior. Notably, the  $\text{Al}_2\text{O}_3/\text{Fe}_2\text{O}_3$  and  $\text{Al}_2\text{O}_3/\text{TiO}_2$  ratios are effective indicators for tracing material sources. The relationship between  $\text{Fe}_2\text{O}_3$  and  $\text{Al}_2\text{O}_3$  is shown in Fig. 4a. The unweathered bedrock samples (carbonate) and soil samples from the SL1, SL2, and XNC profiles have the same positive correlation between  $\text{Fe}_2\text{O}_3$  and  $\text{Al}_2\text{O}_3$  ( $R^2 = 0.95$ ). In these profiles, Al and Fe share the same geochemical behavior, indicating the lack of interference from external materials. Thus, the profiles possess the characteristics of in-situ weathering (Wei et al., 2013). The relationship between  $\text{TiO}_2$  and  $\text{Al}_2\text{O}_3$  is shown in Fig. 4b, wherein  $\text{TiO}_2$  is positively correlated with  $\text{Al}_2\text{O}_3$  in the bedrock and soil samples from the SL1, SL2, and XNC profiles ( $R^2 = 0.98, 0.86, \text{ and } 0.79$ , respectively). This correlation line is the dissolution line of carbonate rock, which suggests that the soil profiles undergo typical in-situ weathering (Young and Nesbitt, 1998). Significant correlations between  $\text{Fe}_2\text{O}_3$  and  $\text{Al}_2\text{O}_3$ , and  $\text{TiO}_2$  and  $\text{Al}_2\text{O}_3$  in the bedrock and soil samples also appeared in the DP profile. This is likely to indicate that DP is also an in-situ weathering profile.

The relationships among  $\text{Al}_2\text{O}_3$ ,  $\text{Fe}_2\text{O}_3$ , and  $\text{SiO}_2$  are shown in Fig. 4c-d. The studied profiles all show that Si decreases while Fe and Al increase in the soil samples. However, the contents of  $\text{Fe}_2\text{O}_3$  and  $\text{SiO}_2$  in the SL1 profile are different from those in the SL2 and XNC profiles (SL1 was enriched in  $\text{Fe}_2\text{O}_3$  and depleted in  $\text{SiO}_2$ ). However, the three profiles all have similar  $\text{Fe}_2\text{O}_3$  and  $\text{SiO}_2$  variation trends. This behavior is also evident in Fig. 4a-b and d. The SL1 profile was more enriched in  $\text{Al}_2\text{O}_3$  and  $\text{Fe}_2\text{O}_3$  and depleted in  $\text{SiO}_2$ , but its variation trend of elements was consistent with that of SL2 and XNC (the scatter plots of the soil samples are distributed on a similar inclined line). Hence, the three profiles may have the same material source and experienced similar pedogenesis processes. Nevertheless, the SL1 profile seems to have experienced a more intense leaching process, which may be due to its geomorphic position (SL1 =  $-1770$  m; SL2 =  $-1730$  m; and XNC =  $-1720$  m). The migration of coarse particles, such as quartz, caused by the leaching of rain and surface water in high-positions (SL1 profile) resulted in the

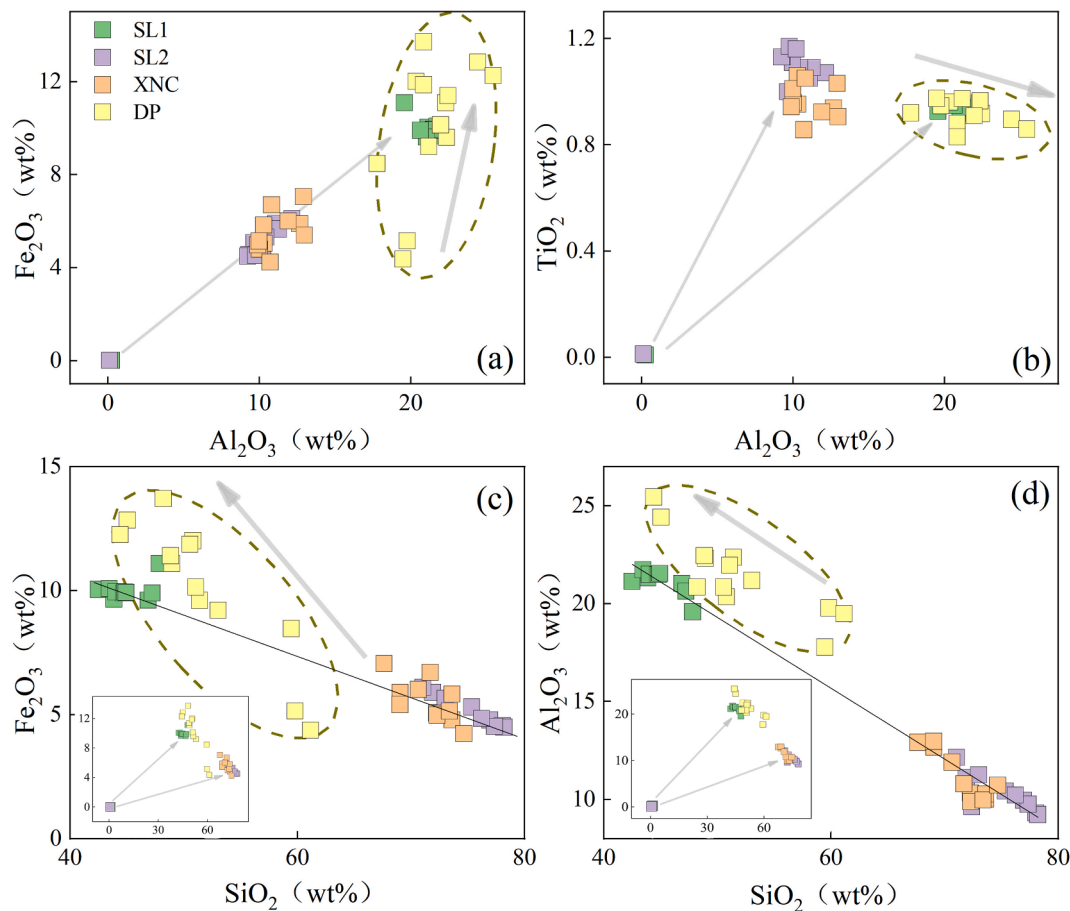


**Fig. 5.** The distribution of (a)  $\text{TiO}_2$  vs.  $\text{Ti/Zr}$ , (b)  $\text{Th}$  vs.  $\text{Th/U}$  (c)  $\text{Nb}$  vs.  $\text{Nb/Ta}$  and (d)  $\text{Nb}$  vs.  $\text{La/Nb}$  for studied soil profiles in Yunnan Plateau, Southwestern China. Horizontal gray band in each plot marks the values in UCC (Taylor and McLennan 1985).  $\text{Ti/Zr} \approx 35.79$ ;  $\text{Th/U} \approx 3.8$ ;  $\text{Nb/Ta} \approx 12$ ;  $\text{La/Nb} \approx 2.4$ . Here we use the  $\text{TiO}_2$  value as  $\text{Ti}$ .

enrichment of Si in lower positions (SL2 and XNC profiles). The  $\text{Fe}_2\text{O}_3$  and  $\text{Al}_2\text{O}_3$  contents were enriched in the SL1 profile because  $\text{Fe}_2\text{O}_3$  and  $\text{Al}_2\text{O}_3$  are more easily enriched in clay minerals, which are not easily leached. The DP profile also has a distinct weathering trend, consisting of a decrease in  $\text{SiO}_2$  content and an increase in  $\text{Al}_2\text{O}_3$  content. However, its inclined trend is different from the other studied profiles.

High field strength elements (HFSEs), such as Ti, Th, U, Nb, Ta, and La, are presumed to be less active and are thus used for indicating provenance (Du et al., 2012; Nasraoui et al., 2000). HFSEs are resistant to weathering, erosion, and deposition, and their contents are likely to be represented in the original rock. As shown in Fig. 5, the weathering profiles of saprolites are markedly different from those of the bedrock of the soil profiles. The bedrock of the SL1 and SL2 profiles have low element concentrations and large variations in element ratios (Fig. 5a, and c-d). This behavior is a result of their bedrocks, which are carbonate. Carbonate rocks dissolve during the pedogenesis process, resulting in a significant volume change and accumulation of elements (Ji et al., 2004a, b). Moreover, the  $\text{Ti/Zr}$  ratio is basically the same in the bedrock and soil profile samples, indicating that the material in the weathering profile may come from the dissolution residue of the bedrock (Huang et al., 2016). As shown in Fig. 5a, the  $\text{Ti/Zr}$  ratio in each profile has a linear relationship with the  $\text{TiO}_2$  concentration, indicating the lack of interference or addition of exogenous materials in the profiles, which is consistent with the characteristics of in-situ weathering. Moreover, as is clear in Fig. 5b, the DP profile samples are clearly different than those of the other three profiles. The SL1, SL2, and XNC profiles are mainly distributed over the upper continental crust (UCC) line ( $\text{Th/U} = 3.8$ ), with a gradually increasing ratio of  $\text{Th/U}$  ( $\text{Th/U} = 4.4\text{--}5.9$ ) (Fig. 5b).

This increase is consistent with the chemical weathering trend ( $R^2 = 0.64$ ) defined by Taylor and McLennan (Taylor and McLennan, 1985). The DP profile samples are also distributed around the UCC line ( $\text{Th/U} = 3.8$ ). However, in the bedrock samples (DP-0) and saprolite (DP-12), the correlation among the samples was weak ( $R^2 = 0.12$ ), and distributed along a weathering line similar to the other three profiles. In Fig. 5c, the four profile samples are distributed near the  $\text{Nb/Ta}$  ratio ( $\text{Nb/Ta} = 14$ ), predominantly above the upper crust  $\text{Nb/Ta}$  ratio ( $\text{Nb/Ta} = 12\text{--}13$ ) (Barth et al., 2000). As shown in Fig. 5d, the SL1, SL2, and XNC profiles are identical and remarkably different from the DP profile. Their correlations between the  $\text{Ta/Nb}$  ratios and Nb concentrations in the soil profiles are weak, and the relationship between these elements and their ratios revealed that the soil profiles had no exotic materials, which may indicate in-situ weathering. Further, the ratios indicate that the SL1, SL2, and XNC profiles that developed from limestone underwent similar weathering processes.

Ti is less chemically active than other elements and is therefore often used as a reference for studying the migration of elements (Ashley and Driese, 2000). The  $\sum\text{REE}/\text{Ti}$  ratio can be used to measure changes in the absolute content of REEs during soil weathering (Dou et al., 2010; Jung et al., 2016). As shown in Fig. 6a, the  $\sum\text{LREE}/\sum\text{HREE}$  and  $\sum\text{REE}/\text{Ti}$  ratios of the SL1, SL2, XNC, and DP profiles are concentrated, and distinct from each other. The SL1 profile has the lowest  $\sum\text{LREE}/\sum\text{HREE}$  value, and its  $\sum\text{REE}/\text{Ti}$  ratio is higher than that of the SL2 and XNC profiles. This suggests that leaching and accumulation may have possibly occurred between the SL1 and SL2 profiles. Further, their  $\sum\text{REE}/\text{Ti}$  ratios decrease with their  $\sum\text{LREE}/\sum\text{HREE}$  ratios, and the contents of the total REEs decrease when the degree of fractionation

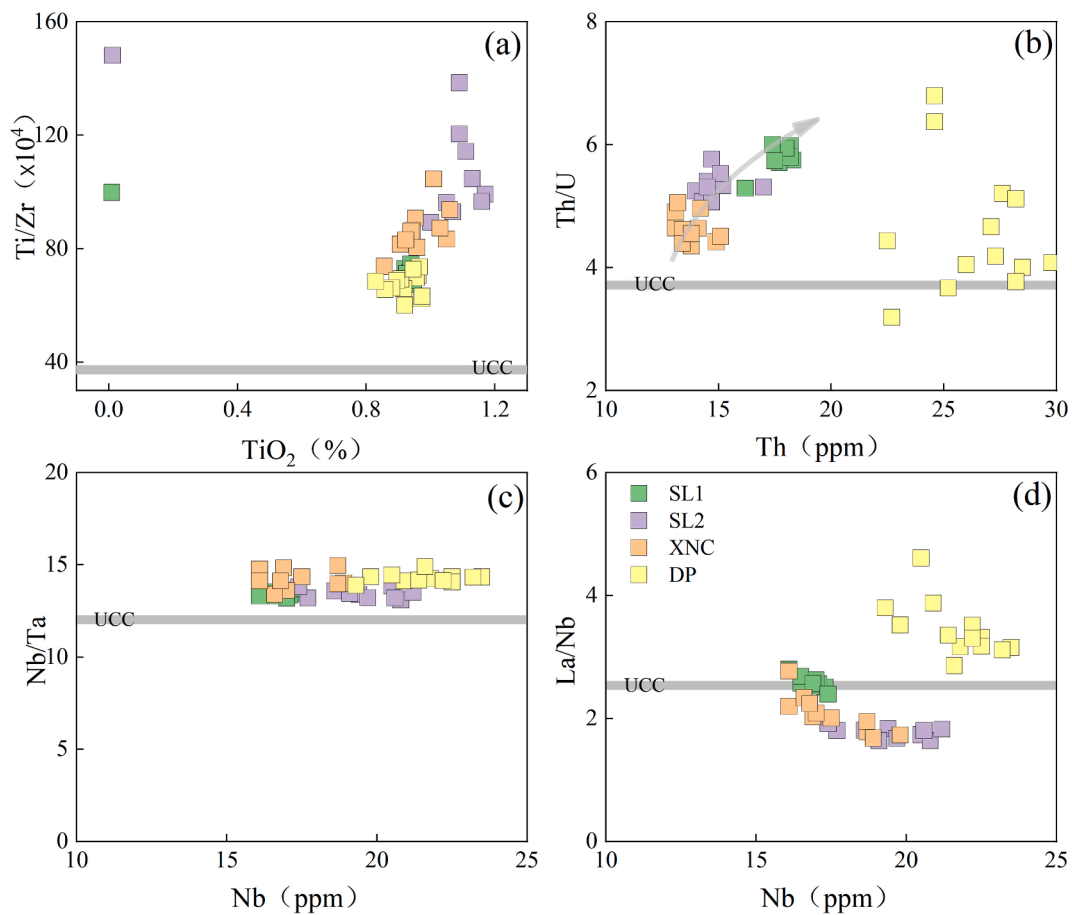


**Fig. 6.** (a) The distribution of  $\sum\text{REE}/\text{Ti}$  vs.  $\sum\text{LREE}/\sum\text{HREE}$  for studied soil profiles in Yunnan Plateau, Southwestern China. The ratio of SL1 and XNC is similar, and there is a significant difference with SL1 and DP. The good tendency for the bedrock to develop into the soil is obvious. There is a leaching trend between SL1 and SL2. (b) The distribution of  $\sum\text{LREE}/\sum\text{HREE}$  vs.  $\delta\text{Ce}$  for studied soil profiles in Yunnan Plateau, Southwestern China. The positive correlations in these profiles are obvious. Here we use the  $\text{TiO}_2$  value as Ti.

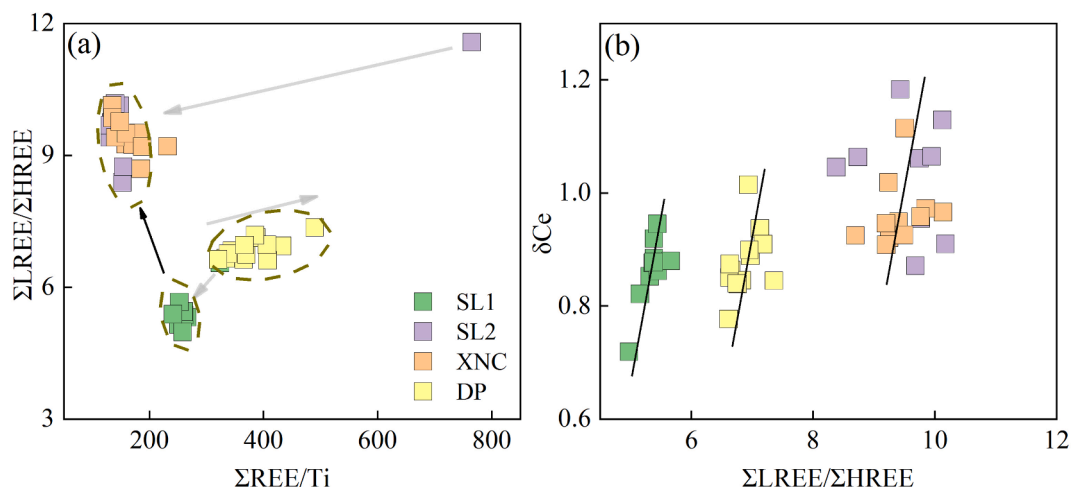


**Fig. 7.** The relationship between (a) CIA and (b) LOI vs.  $\delta^{30}\text{Si}$  and  $\delta^{7}\text{Li}$  isotopic composition for studied soil profiles in Yunnan Plateau, Southwestern China. The CIA,  $\delta^{30}\text{Si}$  and  $\delta^{7}\text{Li}$  value of MORB, Hawaii basalt, Anhui bulk soil, India profile, Xining Loess, Luochuan Loess, UCC and metasedimentary rocks are taken from Gallet et al. (1996), Jahn et al. (2001), Sauzeat et al. (2015), Savage et al. (2010), Teng et al. (2004), Wille et al. (2018), Yang and Zhang (2019), and Ziegler et al. (2005a).

among the REEs increases. For the SL1, SL2, and XNC profiles, the bedrock has a tendency to develop into the soil. The difference in the location of the soil profiles as well as the difference in bedrock for the DP profile showed variation in the  $\sum\text{LREE}/\sum\text{HREE}$  and  $\sum\text{REE}/\text{Ti}$  ratios among the soil profiles. This could be because HREEs are present as

stable compounds in a solution and are preferentially transported downward, whereas the LREEs are easily absorbed by clay minerals due to REE fractionation. The increase in the  $\sum\text{LREE}/\sum\text{HREE}$  value in the upper layer near the surface is consistent with the negative anomaly of surface Ce, and the correlation analysis shows that the  $\sum\text{LREE}/\sum\text{HREE}$

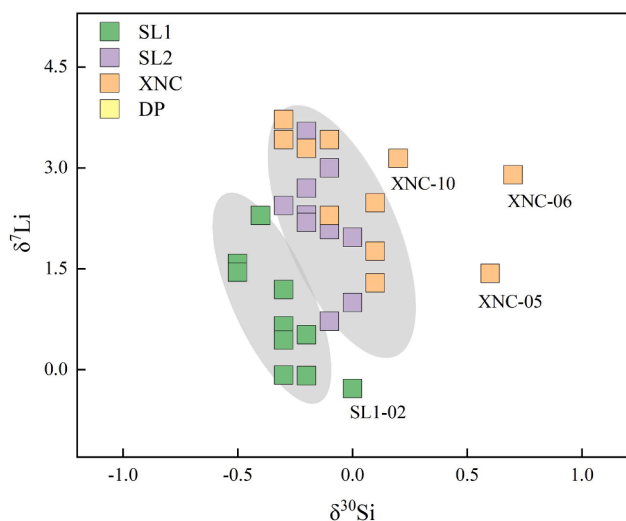


**Fig. 8.** The relationship between Si/Al ratio with (a)  $\delta^{30}\text{Si}$  and (b)  $\delta^7\text{Li}$  isotopic composition and also the relationship between Clay (%) with (a)  $\delta^{30}\text{Si}$  and (b)  $\delta^7\text{Li}$  for studied soil profiles in Yunnan Plateau, Southwestern China. The Si/Al,  $\delta^{30}\text{Si}$  and  $\delta^7\text{Li}$  value of MORB, Hawaii basalt, India profile, Xining Loess, Luochuan Loess, UCC and metasedimentary rocks are taken from Gallet et al. (1996), Jahn et al. (2001), Sauzeat et al. (2015), Savage et al. (2010), Teng et al. (2004), Wille et al. (2018), and Ziegler et al. (2005a).

and  $\delta\text{Ce}$  ratios have a good positive correlation in the SL1 profile (Fig. 6b), with a correlation coefficient of  $R^2 = 0.56$ . Meanwhile, the correlation between  $\delta\text{Ce}$  and  $\sum\text{LREE}/\sum\text{HREE}$  in the three other profiles

is weak, possibly because of the different weathering environments and mineral compositions (Braun et al., 2018).

#### 4.1.2. Si and Li isotope evidence

Aeolian dust, especially Chinese loess, is often regarded as one of the sources of terra rossa in south China. Therefore, the representative Xining Loess, Luochuan Loess, and other crustal components were analyzed to assist the determination of provenance (Gallet et al., 1996; Jahn et al., 2001; Sauzeat et al., 2015; Teng et al., 2004). As seen in Fig. 7a, the  $\delta^{30}\text{Si}$  and Si/Al of the soil samples in the study profiles do not coincide with those in the MORB, Hawaii basalt, and India profiles (Savage et al., 2010; Wille et al., 2018; Ziegler et al., 2005a). Further, as seen in Fig. 7b, with the exception of the bedrock in SL1, the rest of the soil samples are not distributed in the Xining loess, Luochuan Loess, UCC, and Metasedimentary rocks. This same trend is evident in Fig. 8. Therefore, the study profiles have no exogenous materials, such as loess or basalt.

The isotopic evidence illustrated in Fig. 9 reveals the  $\delta^7\text{Li}$  and  $\delta^{30}\text{Si}$  isotopic compositions and frequency distributions of the studied soil profiles. A shift toward the right was observed in the SL1, SL2, and XNC profiles (from high to low elevation) compared with the standard shale (gray highlighted section). A noticeable increase in the heavy isotopic composition of Si and Li isotopes was observed from SL1 to SL2 to XNC. The  $\delta^{30}\text{Si}$  isotopic composition of the DP profile is different from that of these profiles, which show a large  $\delta^{30}\text{Si}$  isotopic composition range, exceeding the distribution of Si isotopes in shale. This result is not due to the addition of extraneous source(s) to the soil samples as is reported in the literature (Von Strandmann et al., 2017), but rather due to the regolith minerals in the lower part of the profile changing minimally, wherein only some soluble minerals, such as feldspar, are decomposed

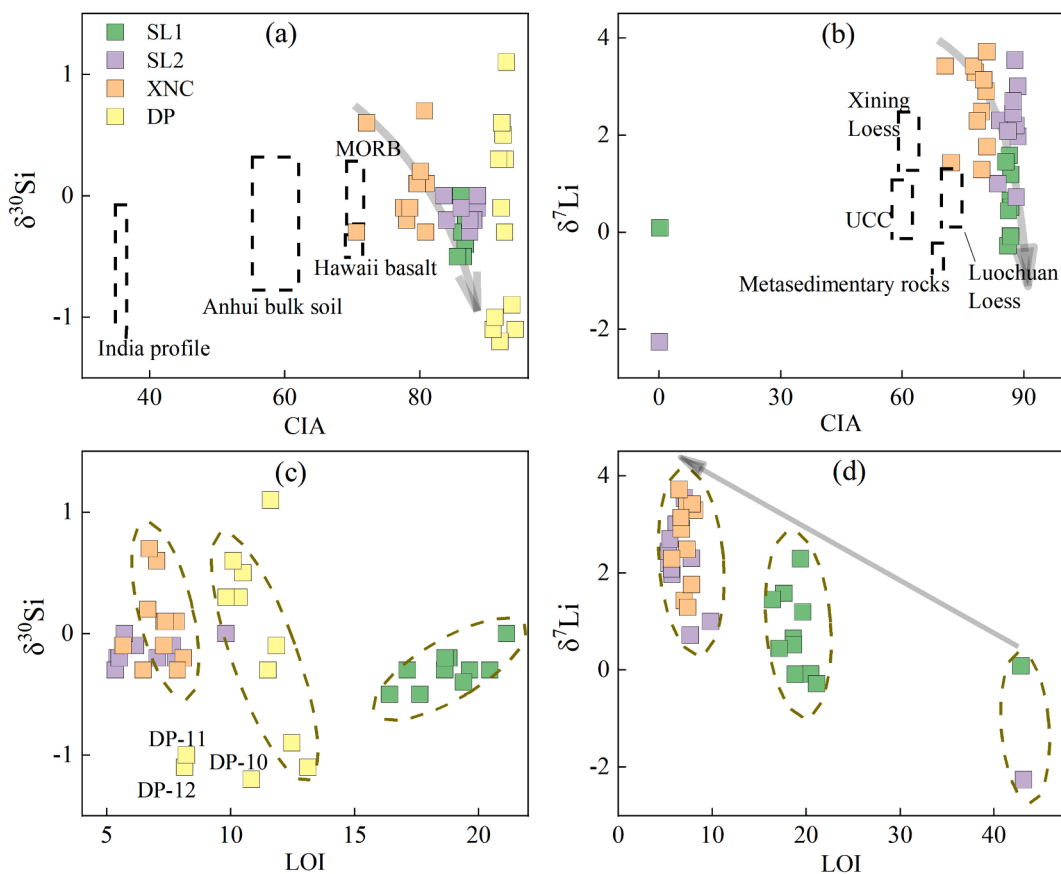


**Fig. 9.** The depth distribution of (a)  $\delta^{30}\text{Si}$  and  $\delta^7\text{Li}$  isotopic composition and (b) Si and Li concentration in four studied soil profiles in Yunnan Plateau, Southwestern China. The vertical shaded bar indicates the UCC value. The Si and  $\delta^{30}\text{Si}$  value ( $[\text{Si}] = 64.1\%$ ,  $\delta^{30}\text{Si} = -0.25 \pm 0.16\text{‰}$ ) are taken from Savage et al. (2013); the Li and  $\delta^7\text{Li}$  value ( $[\text{Li}] = 35 \pm 11 \text{ ppm}$ ,  $\delta^7\text{Li} = 0 \pm 2\text{‰}$ ) are taken from Teng et al. (2004).

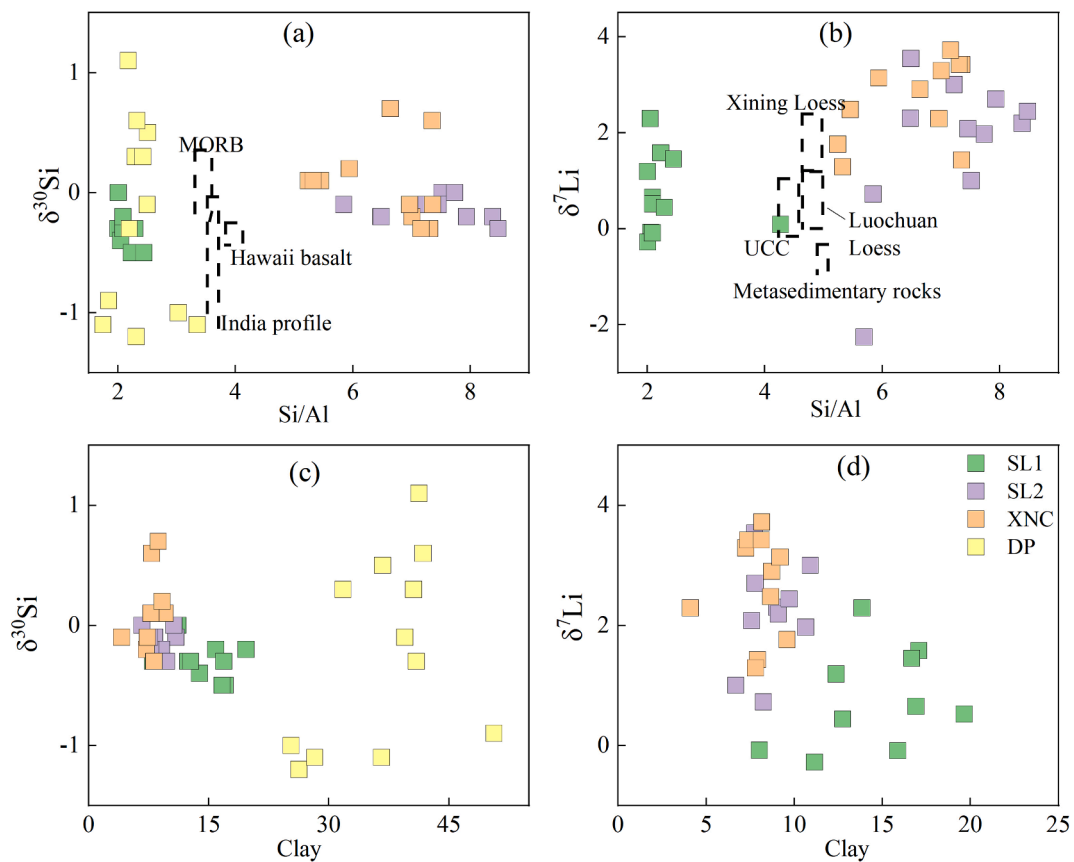


**Fig. 10.** (a) The relationship between  $\delta^{30}\text{Si}$  and  $1/\text{Si}$  ratio for four weathering profiles samples in Yunnan Plateau, Southwestern China. (b) The relationship between  $\delta^7\text{Li}$  and  $1/\text{Li}$  ratio for three weathering profiles samples in Yunnan Plateau, Southwestern China. The small plot showing the influence from phyllosilicates (Ph) and a coarse-grained end-member composed of a mixture of quartz (Qtz) and plagioclase (Pl). All the end-member values come from the literature (Sauzeat et al., 2015). For phyllosilicates (mica, chlorite and clay minerals):  $[\text{Li}] \approx 63$  ppm and  $\delta^7\text{Li} \approx -1$ , for quartz:  $[\text{Li}] \approx 10$  ppm and  $\delta^7\text{Li} \approx +30$  and for plagioclase:  $[\text{Li}] \approx 2$  ppm and  $\delta^7\text{Li} \approx +2.5$ .

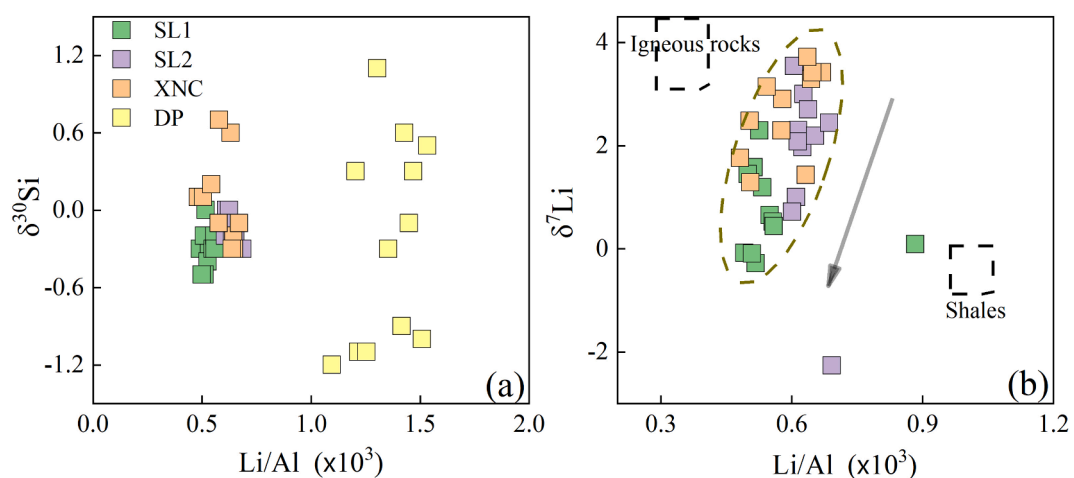


**Fig. 11.** The relationship between  $\delta^{30}\text{Si}$  and  $\delta^7\text{Li}$  isotopic composition for studied soil profiles in Yunnan Plateau, Southwestern China.

by weathering, causing the light Si isotopes in the lower part to be relatively enriched. This confirms that the SL1, SL2, and XNC profiles are derived from a similar source (insoluble residues from carbonate rock dissolution), whereas the DP profile is derived from a different source (shale).

The preferential uptake of isotopically light  $\delta^{28}\text{Si}$  during mineral precipitation may result in typical positive  $\delta^{30}\text{Si}$  values (Ding et al., 2008; Opfergelt et al., 2009). Conversely, the dissolution of secondary

clay minerals may result in low  $\delta^{30}\text{Si}$  values (Cornelis et al., 2010). Studies have indicated that the uppermost soil tends to have low  $\delta^{30}\text{Si}$  values as a result of the recycling of biogenic Si from plants (Ziegler et al., 2005b). However, the studied profiles indicate high  $\delta^{30}\text{Si}$  values on the surface as compared with the bedrock. The increased  $\delta^{30}\text{Si}$  values in the surface may reflect secondary clay minerals, amorphous silica precipitation, and Si uptake by vegetation (Pokrovsky et al., 2006). The formation of developed clay-rich soil leads to the progressive

enrichment in light Si isotope values. Meanwhile, the decrease in  $\delta^{30}\text{Si}$  in the SL1 profile may be related to the increase in clay with depth.

In general, the  $\delta^{30}\text{Si}$  isotopic compositions of the saprolites are lighter than those of the unweathered bedrocks (Bern et al., 2010). However, various chemical weathering conditions (e.g., water chemistry and water-rock ratio) affect the Si isotope signature and  $\delta^{30}\text{Si}$  enriched silica deposits. An increase in  $\delta^{30}\text{Si}$  isotopes, which become isotopically heavier toward the surface, may indicate a change in source. We found that the Si isotopes in the SL1, SL2, and DP profiles increase with depth (Fig. 9) but decrease at the top. As previously mentioned, the profiles have no additional exogenous substances. Thus, the profiles must undergo in-situ weathering and continuous leaching (clay minerals migrate out of the profiles, and quartz mineral content increases). The Si isotope fractionation between quartz and clay minerals (e.g., kaolinite) at equilibrium conditions is 1.6‰ (Opfergelt et al., 2009), and leaching increases the mass of the Si isotope.

During the weathering process, the  $\delta^7\text{Li}$  isotopic compositions of the saprolites are always lighter than those of the unweathered diabase, granite, and basalt (Vigier et al., 2008; Von Strandmann et al., 2006a). The decrease in  $\delta^7\text{Li}$  with increasing depth may indicate a change in source or addition of extraneous sources. However, such a decrease was not found in this study (Fig. 10). Therefore, the study profiles may have a similar source. The high variability in  $\delta^7\text{Li}$  for these soil profiles can be further explained by mineralogy, diffusion-driven redistribution, and leaching. During continental weathering, Li, which is a mobile fluid, is released into water, and  $\delta^7\text{Li}$  is a preferential fluid to rocks (Pistiner and Henderson, 2003; Vigier et al., 2008; Von Strandmann et al., 2006b). Therefore, the  $\delta^7\text{Li}$  values in the saprolite are expected to decrease with increasing degree of weathering toward the surface. The weathering of carbonate rocks is a two-stage model, involving the dissolution and accumulation of carbonate rocks (the insoluble residues), and the weathering of residual soils (Ji et al., 2004a). This weathering results in bedrock that is composed of carbonate rocks with low Li concentrations and light isotopes (Hoefs and Sywall, 1997), diluting the Li concentration and its isotopes in the insoluble residues of the carbonate rocks. Therefore, isotopes become heavier in the bedrock at the soil layer. This trend is not observed in the studied profiles, which all generally increase in  $\delta^7\text{Li}$  values from the bedrock to the surface. This increase could be the result of Li leaching from the surface or diffusion of Li from soil water.

In silicate weathering tracers, the behaviors of Si and Li isotopes are

theoretically the same (Von Strandmann et al., 2017) as both preferentially absorb the lighter isotopes. In Fig. 11, the bulk soil samples of the SL1, XNC (excluding two samples), and SL2 profiles show a consistent negative correlation between  $\delta^7\text{Li}$  and  $\delta^{30}\text{Si}$ , wherein the correlation coefficients are 0.55, 0.32, and 0.19, respectively. The linear array for two isotopes in isotope ratio space is either caused by (1) mixing between end members with distinct isotopic compositions or (2) coupled fractionation between the two elements induced by one or more physicochemical process (Tipper et al., 2012). Some correlations of Si-Li isotopes are found in basalt rivers and interpreted as differences in kinetics and control of differences in isotopic fractionation (Opfergelt and Delmelle, 2012). Notably, the negative correlation of Si-Li isotopes should not be regarded as a mixture of end members because linear correlations in geochemical datasets are frequently inferred as binary mixtures, and a binary mixing line is described by a hyperbola (Tipper et al., 2012). However, a linear relationship is a special case of a mixing hyperbola where the element ratios of both end members are similar. In Fig. 11, we cannot determine a condition involving two end-elements, and the three profiles show significant weathering characteristics. We believe that this negative correlation is controlled by physicochemical processes associated with clays or oxides and an increase in the degree of leaching and organic matter content.

#### 4.2. Isotopes fractionation during geochemical weathering processes

##### 4.2.1. $\delta^{30}\text{Si}$ , $\delta^7\text{Li}$ , CIA value and LOI contents in terra rossa

CIA values are used to determine the chemical weathering intensity within a soil profile (Maynard, 1992). The relationships between the  $\delta^{30}\text{Si}$  isotopic compositions and CIA are shown in Fig. 7a. Here, the  $\delta^{30}\text{Si}$  isotopic values of the soil profiles (except for the bedrock and saprolite samples) are weakly negatively correlated with the CIA. However, the slopes of the correlation between the SL1, SL2, and XNC profiles (carbonate) are notably different from the DP profile (shale). The relationship between the two groups in this study shows that they are derived from the weathering of bedrock and have their own evolutionary characteristics. A similar negative correlation was reported for the CIA and  $\delta^{30}\text{Si}$  values of bulk soil in Yang and Zhang (Yang and Zhang, 2019). Thus, the  $\delta^{30}\text{Si}$  values of bulk soils are highly related to the degree of chemical weathering. Similarly, the  $\delta^7\text{Li}$  isotopic values of the SL1, SL2, and XNC profiles are weakly negatively correlated with CIA (except for a

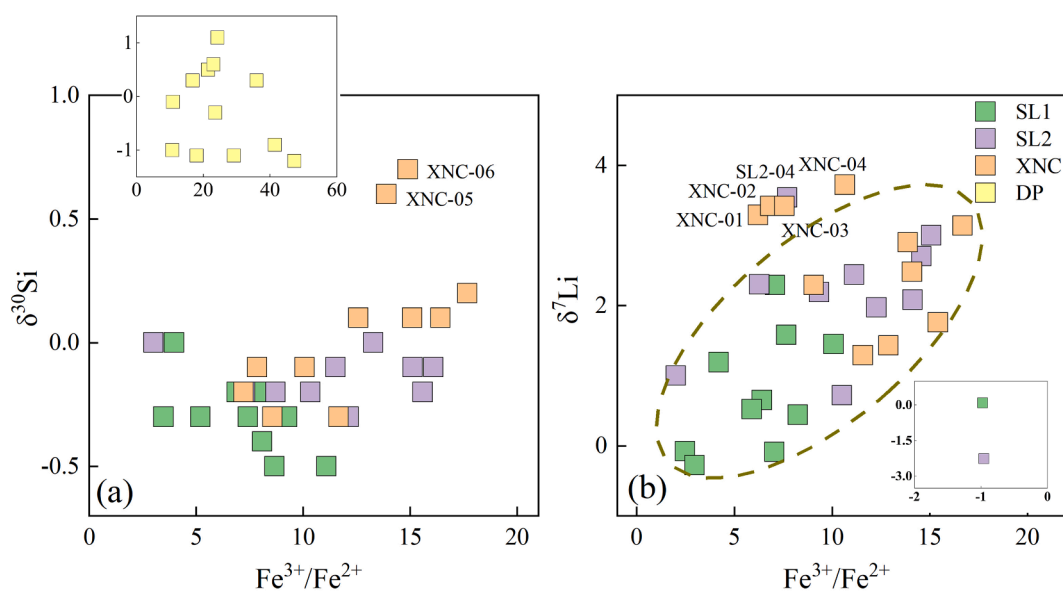
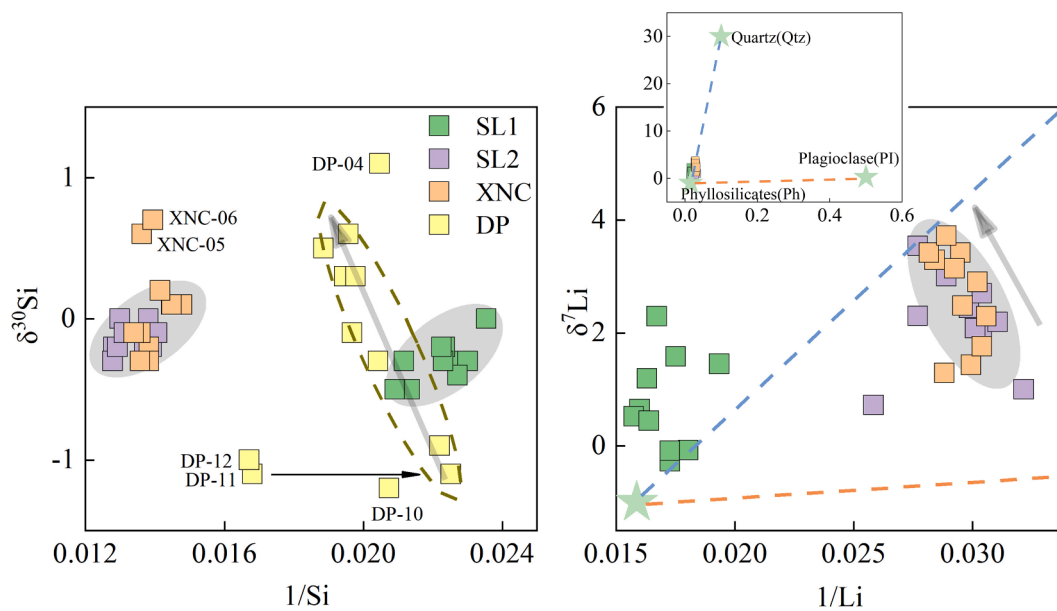


Fig. 12. The relationship between Li/Al ratio with (a)  $\delta^{30}\text{Si}$  and (b)  $\delta^7\text{Li}$  isotopic composition for studied soil profiles in Yunnan Plateau, Southwestern China. The little plot represents the weathering trends (first increase and then decline) of the SL1 and SL2 samples. The blue arrow indicates weathering trend which has been pointed out by Dellinger et al. (2014). (For interpretation of the references to colour in this figure legend, the reader is referred to the web version of this article.)



**Fig. 13.** The relationship between  $\text{Fe}^{3+}/\text{Fe}^{2+}$  concentration with (a)  $\delta^{30}\text{Si}$  and (b)  $\delta^7\text{Li}$  isotopic composition for studied soil profiles in Yunnan Plateau, South-western China.

few samples). This negative correlation between  $\delta^7\text{Li}$  and CIA has been reported in meta-sedimentary rocks in the British Caledonides and the Catalina Schist (Penniston-Dorland et al., 2012; Qiu et al., 2009), and in a binary isotopic mixing trend in the desert loess deposits (Sauzeat et al., 2015). These overlying carbonate rock profiles have unique properties and are distinct from other weathered profiles.

A commonly used tool for determining humus content in soil is the LOI method. High LOI values reflect the influence of high water-bearing minerals, such as clay and organic matter. The relationships between  $\delta^{30}\text{Si}$  isotopic compositions and LOIs are illustrated in Fig. 7c. The SL1 profile has the highest LOI value with an inclined trend, suggesting that  $\delta^{30}\text{Si}$  isotopic fractionation increases with LOI. This may be due to biological influences and the preferential uptake of isotopically light  $\delta^{30}\text{Si}$  during mineral precipitation, which may result in typical positive  $\delta^{30}\text{Si}$  values (Ding et al., 2008; Opfergelt et al., 2009). The SL1 profile is located under a high vegetation cover, consisting mainly of shrubs and herbaceous plants. The DP profile showed a distinct weathering trend with a low soil profile close to the bedrock. Meanwhile, the rest of the soil saprolites showed a declining trend, indicating that the  $\delta^{30}\text{Si}$  isotopic composition decreases with increasing LOI. The XNC profile showed a similar trend, and the SL2 profile showed no obvious trend. The relationship between the  $\delta^7\text{Li}$  isotopic composition and the LOI (Fig. 7d) revealed a weathering trend from unweathered bedrock with a high LOI in developed soil saprolites in the SL1, SL2, and XNC profiles with decreasing LOI values. Here, the soil profiles showed a noticeable declining trend in  $\delta^7\text{Li}$  isotopic composition. This may be related to the clay mineral content in the soil. The decrease in LOI indicates that the decrease in clay mineral contents, which have light lithium isotope compositions, leads to a positive  $\delta^7\text{Li}$ .

#### 4.2.2. $\delta^{30}\text{Si}$ , $\delta^7\text{Li}$ , Si/Al ratio, and clay contents in terra rossa

The Si/Al ratio is used to measure “clayeyness” and as a source of soil development (Huh et al., 2001). Given their behavior, the Si/Al ratio can be used as an index for weathering intensity (Bouchez et al., 2011; Lupker et al., 2011). For example, the Si/Al ratio is small in strongly weathered soil. The relationship between  $\delta^{30}\text{Si}$  isotopic composition and Si/Al ratio indicates that the SL1 and DP profiles have relatively fine grain sizes, which seems to have no clear effect on the  $\delta^{30}\text{Si}$  isotopic fractionation. However, the DP profile showed a relatively large isotopic composition range (Fig. 8a). Conversely, the SL2 and XNC profiles have

large particles, indicating a declining trend (Fig. 8a). This finding suggests that grain size influences  $\delta^{30}\text{Si}$  isotopic fractionation in the SL2 and XNC profiles. Further, the relationship between  $\delta^{30}\text{Si}$  isotopic composition and clay content indicates that the DP profile samples have large clay contents and the largest isotopic range (Fig. 8c). However, the  $\delta^{30}\text{Si}$  isotope values of the SL1, SL2, and XNC profiles (except for two samples) decrease with increasing clay content. This supports the current consensus that weathered clay minerals are lighter in  $\delta^{30}\text{Si}$  isotope values than in unweathered parent rocks (Bern et al., 2010; Qiu et al., 2009). Furthermore, shale Si isotope compositions are negatively correlated with the Al/Si ratio (Savage et al., 2013). This relationship reflects the implication of  $\delta^{30}\text{Si}$  on soil evolution with changing physicochemical properties.

The Li isotope compositions of the studied soil profiles as a function of the Si/Al ratio can be used as a proxy for grain size to determine their source and weathering intensities (Bouchez et al., 2011; Opfergelt and Delmelle, 2012). A soil profile with a low Si/Al value (<0.15) is considered weathered fine sized clayed soil, whereas a soil profile with a high Si/Al value is considered to be extremely weathered clayed soil. The relationship between  $\delta^7\text{Li}$  isotopic composition and Si/Al ratio is illustrated in Figs. 8b and 10b. Overall, this relationship shows that the SL1 profile has relatively small clay size particles, which seem to have no effect on  $\delta^7\text{Li}$  isotopic fractionation. Meanwhile, the SL2 and XNC profiles have relatively large grain sizes, which seem to affect  $\delta^7\text{Li}$  isotopic fractionation, as indicated by the inclining trend, which indicates that grain size increases with the degree of  $\delta^7\text{Li}$  isotopic fractionation. Further, the relationship between  $\delta^7\text{Li}$  isotopic composition and clay content indicates that all the sample points in the three profiles are dispersed (Fig. 8d), but their  $\delta^7\text{Li}$  isotopic values are approximately inverse to their clay contents. This inverse relationship is consistent with the formation of light Li isotopes preferentially incorporated by clay minerals during weathering and the migration of heavy Li isotopes within aqueous solutions (Dellinger et al., 2014; Millot et al., 2010; Von Strandmann et al., 2006a).

#### 4.2.3. $\delta^{30}\text{Si}$ , $\delta^7\text{Li}$ , Li/Al ratio, and $\text{Fe}^{3+}/\text{Fe}^{2+}$ ratio in terra rossa

Li and Si isotopic compositions can be used with the Li/Al ratio to track sediment grain size, source indicators, and chemical weathering processes (Fig. 12). Herein, no obvious correlation trend was observed in the relationship between  $\delta^{30}\text{Si}$  and the Li/Al ratio (Fig. 12a) with the

exception of the DP profile (shale) being remarkably different from the other profiles (carbonate), which have large isotopic compositions and large Li/Al ratios. This result confirms that the DP profile originates from different sources (shale), and that the large isotopic fractionation observed may be due to biological weathering processes (Ding et al., 2008; Opfergelt et al., 2008; Steinhöfel et al., 2017; Ziegler et al., 2005a).

The relationship between  $\delta^7\text{Li}$  isotopic composition and the Li/Al ratio showed an inclined weathering trend in the SL1, SL2, and XNC profiles (Fig. 12b), which is the same as the theoretical fully weathered component trend determined by Dellinger et al. (2014). Hence, Li/Al decreases with decreasing  $\delta^7\text{Li}$  values. Further, the soil profiles are two end members (igneous rock and shales) mixed together with relatively small isotopic variation, indicating that the soil samples from the study profiles are from the same source, that is, carbonate rocks. The bedrock samples for the SL1 and SL2 profiles are significantly different from the rest of the soil profiles with large Li/Al ratios.

In soils, Fe initially exists in primary minerals and bedrocks. However, during chemical weathering, Fe is usually mobilized via proton promoted, ligand controlled, or reductive dissolution. The mean values of Fe concentrations in the studied soil profiles are 5.12, 5.55, 10.01, and 10.64 for the SL2, XNC, SL1, and DP profiles, respectively. In all the soil profiles,  $\text{Fe}^{2+}$  is primarily present in ferromagnesian silicates, and  $\text{Fe}^{3+}$  is mostly in the form of Fe oxides and hydroxides. Fe reactions during chemical weathering are largely dependent on the pH-Eh and its current oxidation state. In general, oxidizing and alkaline conditions promote Fe precipitation, whereas acidic and reducing conditions favor the solution of Fe compounds. Therefore, acidic soil tends to have high levels of soluble inorganic Fe compounds. The presence and exchange of Fe oxides in secondary clay fractionation may contribute to the light Si isotope composition of clay fractions because of Si adsorption onto Fe oxides (Swedlund and Webster, 1999), which favors isotopically light  $\delta^{30}\text{Si}$  (Opfergelt et al., 2008). Therefore, a relationship between soil  $\delta^{30}\text{Si}$  isotopic composition and  $\text{Fe}^{3+}/\text{Fe}^{2+}$  redox exchange was observed (Fig. 13). Fig. 13 also highlights a weak positive correlation in the SL2, XNC, and DP profiles and a negative correlation in the SL1 profile. Conversely, the relationship between soil  $\delta^7\text{Li}$  isotopic composition and  $\text{Fe}^{3+}/\text{Fe}^{2+}$  exchange (Fig. 13), indicating a strong positive correlation and suggesting that secondary clay fractions involving  $\text{Fe}^{3+}/\text{Fe}^{2+}$  redox exchange increases with  $\delta^7\text{Li}$  isotopic composition in the SL1, SL2, and XNC profiles during weathering.

## 5. Conclusions

This study investigated the mineralogy, geochemistry, and isotopic composition of Li and Si for four soil profiles of lateritic weathering over a karst area in the Yunnan Plateau, southwestern China. The mineralogical evidence indicated that the soil profiles have the characteristic features of a red clay soil that is acidic and organic-rich from a subtropical humid climate. The mineral assemblages of the profiles were mainly composed of quartz and clay minerals derived from clastic materials. During the chemical weathering process, the elemental distributions in these laterite soils were controlled by dissolution, accumulation, and leaching, which were promoted by physicochemical conditions. Based on the geochemical evidence, the SL1, SL2, and XNC profiles had good inheritance of the underlying carbonate bedrock of the same source and were derived from in-situ weathering. Meanwhile, the DP profile was considerably different as it was derived from silicate (shale) and had a distinct weathering trend. The isotopic evidence indicated that Si and Li isotopes in the SL1, SL2, and XNC profiles were mainly affected by clay mineral content, organic matter content, and degree of oxidation. The heavier isotopes of Si and Li increased with changes in landform and after the leaching of clay minerals. A linear negative correlation between the isotope ratios suggested that the weathering processes were less affected by biological fractionation, and more by the physicochemical processes associated with clay or oxide,

leaching, and increasing organic matter. This study shows that Si and Li isotopic systems, combined with mineralogical and geochemical evidence, are good origin and evolution indicators for complex lateritic soils in karst areas and can therefore be used in pedogenesis.

## Declaration of Competing Interest

The authors declare that they have no known competing financial interests or personal relationships that could have appeared to influence the work reported in this paper.

## Acknowledgements

We are indebted to Prof. Shijie Wang discussion and suggestions about this study. We thank Dr. Chuan Yin for his assistance preparation of background map and Ms. Haiou Ma for her assistance with field sampling and analysis. This work was supported by the National Natural Science Foundation of China (NSFC) grants (41473122, 41073096), the National Key Basic Research Program of China (2013CB956702) and the Hundred Talents Program of the Chinese Academy of Sciences.

## Appendix A. Supplementary material

Supplementary data to this article can be found online at <https://doi.org/10.1016/j.catena.2020.105022>.

## References

- Abraham, K., Opfergelt, S., Fripiat, F., Cavagna, A.J., De Jong, J., Foley, S.F., Andre, L., Cardinal, D., 2008.  $\delta^{30}\text{Si}$  and  $\delta^{29}\text{Si}$  determinations on USGS BHVO-1 and BHVO-2 reference materials with a new configuration on a Nu plasma multi-collector ICP-MS. *Geostandard. Geanal. Res.* 32, 193–202.
- Alexandre, A., Meunier, J., Colin, F., Koud, J., 1997. Plant impact on the biogeochemical cycle of silicon and related weathering processes. *Geochim. Cosmochim. Acta* 61, 677–682.
- Anderson, S.P., Blum, J., Brantley, S.L., Chadwick, O., Chorover, J., Derry, L.A., Drever, J.I., Hering, J.G., Kirchner, J.W., Kump, L., 2004. Proposed initiative would study Earth's weathering engine. *Eos Trans. Am. Geophys. Union* 85, 265.
- Ashley, G.M., Driese, S.G., 2000. Paleopedology and paleohydrology of a volcanoclastic paleosol interval: implications for early pleistocene stratigraphy and paleoclimate record, Olduvai Gorge, Tanzania. *J. Sediment. Res.* 70, 1065–1080.
- Barth, M., McDonough, W.F., Rudnick, R.L., 2000. Tracking the budget of Nb and Ta in the continental crust. *Chem. Geol.* 165, 197–213.
- Bates, R.L., Jackson, J.A., 1987. *Glossary of geology*. Am. Geol. Inst. 788 pp.
- Blackburn, G., 1983. Soils. In: Tyler, M.J., Twidale, C.R., Ling, J.K., Holmes, J.W. (Eds.), *Natural History of the South East*. Royal Society of South Australia, Adelaide, Australia, pp. 40–48.
- Bern, C.R., Brzezinski, M.A., Beucher, C.P., Ziegler, K., Chadwick, O.A., 2010. Weathering, dust, and biocycling effects on soil silicon isotope ratios. *Geochim. Cosmochim. Acta* 74, 876–889.
- Bouchez, J., Gaillardet, J., Francelanord, C., Maurice, L., Dutrammaia, P., 2011. Grain size control of river suspended sediment geochemistry: Clues from Amazon River depth profiles. *Geochim. Geophys. Geosys.* 12.
- Bouman, C., Elliott, T., Vroon, P.Z., 2004. Lithium inputs to subduction zones. *Chem. Geol.* 212, 59–79.
- Brantley, S.L., Goldhaber, M.B., Ragnarsdottir, K.V., 2007. Crossing disciplines and scales to understand the critical zone. *Elements* 3, 307–314.
- Braun, J.-J., Pagel, M., Herbillin, A., Rosin, C., 1993. Mobilization and redistribution of REEs and thorium in a syenitic lateritic profile: a mass balance study. *Geochim. Cosmochim. Acta* 57, 4419–4434.
- Braun, J.-J., Riotte, J., Battacharya, S., Violette, A., Oliva, P., Prunier, J., Maréchal, J.C., Ruiz, L., Audry, S., Subramanian, S., 2018. REY-Th-U dynamics in the critical zone: combined influence of reactive bedrock accessory minerals, authigenic phases, and hydrological sorting (Mule Hole Watershed, South India). *Geochem. Geophys. Geosys.* 19, 1611–1635.
- Capo, R.C., Stewart, B.W., Chadwick, O.A., 1998. Strontium isotopes as tracers of ecosystem processes: theory and methods. *Geoderma* 82, 197–225.
- Cooke, M.J., Stern, L.A., Banner, J.L., Mack, L.E., 2007. Evidence for the silicate source of relict soils on the Edwards Plateau, central Texas. *Quaternary Res.* 67, 275–285.
- Cornelis, J., Delvaux, B., Georg, R., Lucas, Y., Ranger, J., Opfergelt, S., 2010. Tracing the origin of dissolved silicon transferred from various soil-plant systems towards rivers: a review. *Biogeosciences* 8, 89–112.
- Dauphas, N., John, S.G., Rouxel, O., 2017. Iron isotope systematics. *Rev. Mineral. Geochem.* 82, 415–510.
- Dellinger, M., Gaillardet, J., Bouchez, J., Calmels, D., Galy, V., Hilton, R.G., Louvat, P., Francelanord, C., 2014. Lithium isotopes in large rivers reveal the cannibalistic

- nature of modern continental weathering and erosion. *Earth Planet. Sc. Lett.* 401, 359–372.
- Ding, T., Wan, D., Wang, C., Zhang, F., 2004. Silicon isotope compositions of dissolved silicon and suspended matter in the Yangtze River, China. *Geochim. Cosmochim. Acta* 68, 205–216.
- Ding, T.P., Zhou, J.X., Wan, D.F., Chen, Z.Y., Wang, C.Y., Zhang, F., 2008. Silicon isotope fractionation in bamboo and its significance to the biogeochemical cycle of silicon. *Geochim. Cosmochim. Acta* 72, 1381–1395.
- Dou, Y., Yang, S., Liu, Z., Cliff, P.D., Shi, X., Yu, H., Berne, S., 2010. Provenance discrimination of siliciclastic sediments in the middle Okinawa Trough since 30 ka: Constraints from rare earth element compositions. *Mar. Geol.* 275, 212–220.
- Driese, S.G., Jacobs, J.R., Nordt, L.C., 2003. Comparison of modern and ancient Vertisols developed on limestone in terms of their geochemistry and parent material. *Sediment Geol.*
- Du, X., Rate, A.W., Gee, M.A.M., 2012. Redistribution and mobilization of titanium, zirconium and thorium in an intensely weathered lateritic profile in Western Australia. *Chem. Geol.* 330–331, 101–115.
- Durn, G., Ottner, F., Slovenec, D., 1999. Mineralogical and geochemical indicators of the polygenetic nature of terra rossa in Istria, Croatia. *Geoderma* 91, 125–150.
- Feng, J.L., Cui, Z.J., Zhu, L.P., 2009. Origin of terra rossa over dolomite on the Yunnan-Guizhou Plateau, China. *Geochim. J.* 43, 151–166.
- Gallet, S., Jahn, B., Torii, M., 1996. Geochemical characterization of the Luochuan loess-paleosol sequence, China, and paleoclimatic implications. *Chem. Geol.* 133, 67–88.
- Georg, R.B., Reynolds, B.C., Frank, M., Halliday, A.N., 2006. Mechanisms controlling the silicon isotopic compositions of river waters. *Earth Planet. Sc. Lett.* 249, 290–306.
- Hoefs, J., Sywall, M., 1997. Lithium isotope composition of quaternary and tertiary biogenic carbonates and a global lithium isotope balance. *Geochim. Cosmochim. Acta* 61, 2679–2690.
- Huang, W.S., Jien, S.H., Tsai, H., Hseu, Z.Y., Huang, S.T., 2016. Soil evolution in a tropical climate: an example from a chronosequence on marine terraces in Taiwan. *Catena* 139, 61–72.
- Huh, Y., Chan, L., Edmond, J.M., 2001. Lithium isotopes as a probe of weathering processes: Orinoco River. *Earth Planet. Sc. Lett.* 194, 189–199.
- Jackson, M.L., 1982. Eolian influence on terra rossa soils of Italy traced by quartz oxygen isotope ratio. *Int. Clay Conf.*
- Jahn, B., Gallet, S., Han, J., 2001. Geochemistry of the Xining, Xifeng and Jixian sections, Loess Plateau of China: eolian dust provenance and paleosol evolution during the last 140 ka. *Chem. Geol.* 178, 71–94.
- Ji, H., Wang, S., Ouyang, Z., Zhang, S., Sun, C., Liu, X., Zhou, D., 2004a. Geochemistry of red residua underlying dolomites in karst terrains of Yunnan-Guizhou Plateau. *Chem. Geol.* 203, 1–27.
- Ji, H., Wang, S., Ouyang, Z., Zhang, S., Sun, C., Liu, X., Zhou, D., 2004b. Geochemistry of red residua underlying dolomites in karst terrains of Yunnan-Guizhou Plateau. *Chem. Geol.* 203, 29–50.
- Jung, H., Lim, D., Jeong, D., Xu, Z., Li, T., 2016. Discrimination of sediment provenance in the Yellow Sea: Secondary grain-size effect and REE proxy. *J. Asian Earth Sci.* 123, 78–84.
- Kennedy, M.J., Chadwick, O.A., Vitousek, P.M., Derry, L.A., Hendricks, D.M., 1998. Changing sources of base cations during ecosystem development, Hawaiian Islands. *Geology* 26, 1015–1018.
- Kisakurek, B., Widdowson, M., James, R.H., 2004. Behaviour of Li isotopes during continental weathering: the Bidar laterite profile. *India. Chem. Geol.* 212, 27–44.
- La Rocha, C.L.D., 2002. Measurement of silicon stable isotope natural abundances via multicollector inductively coupled plasma mass spectrometry (MC-ICP-MS). *Geochim. Geophys. Geosys.* 3, 1–8.
- Lupker, M., Francelanord, C., Lave, J., Bouchez, J., Galy, V., Metivier, F., Gaillardet, J., Lartiges, B., Mugnier, J., 2011. A Rouse-based method to integrate the chemical composition of river sediments: application to the Ganga basin. *J. Geophys. Res.* 116, 1159.
- Maynard, J., 1992. Chemistry of modern soils as a guide to interpreting Precambrian paleosols. *J. Geol.* 100, 279–289.
- Mee, A.C., Bestland, E.A., Spooner, N.A., 2004. Age and origin of Terra Rossa soils in the Coonawarra area of South Australia. *Geomorphology* 58, 1–25.
- Millot, R., Vigier, N., Gaillardet, J., 2010. Behaviour of lithium and its isotopes during weathering in the Mackenzie Basin, Canada. *Geochim. Cosmochim. Acta* 74, 3897–3912.
- Muhs, D.R., Budahn, J.R., 2009. Geochemical evidence for African dust and volcanic ash inputs to terra rossa soils on carbonate reef terraces, northern Jamaica, West Indies. *Quatern. Int.* 196, 13–35.
- Nasraoui, M., Toulkeridis, T., Clauer, N., Bilal, E.J.C.G., 2000. Differentiated hydrothermal and meteoric alterations of the Lueshe carbonate complex (Democratic Republic of Congo) identified by a REE study combined with a sequential acid-leaching experiment. *Chem. Geol.* 165, 109–132.
- Nesbitt, H.W., Young, G.M., 1982. Early Proterozoic climates and plate motions inferred from major chemistry of lites. *Nature* 299, 715–717.
- Nihlen, T., Olsson, S., 1995. Influence of Eolian dust on soil formation in the Aegean area. *Z. Geomorphol.* 39 (3), 341–361.
- Opfergelt, S., De Bournonville, G., Cardinal, D., Andre, L., Delstanche, S., Delvaux, B., 2009. Impact of soil weathering degree on silicon isotopic fractionation during adsorption onto iron oxides in basaltic ash soils. *Cameroon. Geochim. Cosmochim. Acta* 73, 7226–7240.
- Opfergelt, S., Delmelle, P., 2012. Silicon isotopes and continental weathering processes: assessing controls on Si transfer to the ocean. *C.R. Geosci.* 344, 723–738.
- Opfergelt, S., Delvaux, B., Andre, L., Cardinal, D., 2008. Plant silicon isotopic signature might reflect soil weathering degree. *Biogeochemistry* 91, 163–175.
- Penniston-Dorland, S.C., Bebout, G.E., Von Strandmann, P.A.E.P., Elliott, T., Sorensen, S., 2012. Lithium and its isotopes as tracers of subduction zone fluids and metamorphic processes: Evidence from the Catalina Schist, California, USA. *Geochim. Cosmochim. Acta* 77, 530–545.
- Pistiner, J.S., Henderson, G.M., 2003. Lithium-isotope fractionation during continental weathering processes. *Earth Planet. Sc. Lett.* 214, 327–339.
- Pokrovsky, O.S., Schott, J., Dupre, B., 2006. Trace element fractionation and transport in boreal rivers and soil porewaters of permafrost-dominated basaltic terrain in Central Siberia. *Geochim. Cosmochim. Acta* 70, 3239–3260.
- Qiu, L., Rudnick, R.L., McDonough, W.F., Merriman, R.J., 2009. Li and  $^6\text{Li}$  in mudrocks from the British Caledonides: Metamorphism and source influences. *Geochim. Cosmochim. Acta* 73, 7325–7340.
- Rudnick, R.L., Tomascak, P.B., Njo, H.B., Gardner, L.R., 2004. Extreme lithium isotopic fractionation during continental weathering revealed in saprolites from South Carolina. *Chem. Geol.* 212, 45–57.
- Sauzeat, L., Rudnick, R.L., Chauvel, C., Garcon, M., Tang, M., 2015. New perspectives on the Li isotopic composition of the upper continental crust and its weathering signature. *Earth Planet. Sc. Lett.* 428, 181–192.
- Savage, P.S., Georg, R.B., Armutage, R.M.G., Williams, H.M., Halliday, A.N., 2010. Silicon isotope homogeneity in the mantle. *Earth Planet. Sc. Lett.* 295, 139–146.
- Savage, P.S., Georg, R.B., Williams, H.M., Halliday, A.N., 2013. The silicon isotope composition of the upper continental crust. *Geochim. Cosmochim. Acta* 109, 384–399.
- Steinwoelfel, G., Breuer, J., Von Blanckenburg, F., Horn, I., Sommer, M., 2017. The dynamics of Si cycling during weathering in two small catchments in the Black Forest (Germany) traced by Si isotopes. *Chem. Geol.* 466, 389–402.
- Swedlund, P.J., Webster, J.G., 1999. Adsorption and polymerisation of silicic acid on ferrihydrite, and its effect on arsenic adsorption. *Water Res.* 33, 3413–3422.
- Taylor, S.R., McLennan, S.M., 1985. *The continental crust: Its composition and evolution*. Oxford, Blackwell's, 312 p.
- Teng, F., McDonough, W.F., Rudnick, R.L., Dalpe, C., Tomascak, P.B., Chappell, B.W., Gao, S., 2004. Lithium isotopic composition and concentration of the upper continental crust. *Geochim. Cosmochim. Acta* 68, 4167–4178.
- Tipper, E.T., Calmels, D., Gaillardet, J., Louvat, P., Capmas, F., Dubacq, B., 2012. Positive correlation between Li and Mg isotope ratios in the river waters of the Mackenzie Basin challenges the interpretation of apparent isotopic fractionation during weathering. *Earth Planet. Sc. Lett.* 333, 35–45.
- Tsai, H., Hseu, Z.-Y., Huang, W.-S., Chen, Z.-S., 2007. Pedogenic approach to resolving the geomorphic evolution of the Pakua river terraces in central Taiwan. *Geomorphology* 83, 14–28.
- Tsai, P., You, C., Huang, K., Chung, C.H., Sun, Y., 2014. Lithium distribution and isotopic fractionation during chemical weathering and soil formation in a loess profile. *J. Asian Earth Sci.* 87, 1–10.
- Ushikubo, T., Kita, N.T., Cavoie, A.J., Wilde, S.A., Rudnick, R.L., Valley, J.W., 2008. Lithium in Jack Hills zircons: Evidence for extensive weathering of Earth's earliest crust. *Earth Planet. Sc. Lett.* 272, 666–676.
- Vigier, N., Decarreau, A., Millot, R., Carignan, J., Petit, S., Francelanord, C., 2008. Quantifying Li isotope fractionation during smectite formation and implications for the Li cycle. *Geochim. Cosmochim. Acta* 72, 780–792.
- Von Strandmann, P.A.E.P., Burton, K.W., James, R.H., Van Calsteren, P., Gislason, S.R., Mokadem, F., 2006a. Riverine behaviour of uranium and lithium isotopes in an actively glaciated basaltic terrain. *Earth Planet. Sc. Lett.* 251, 134–147.
- Von Strandmann, P.A.E.P., Burton, K.W., James, R.H., Van Calsteren, P., Gislason, S.R., Sigfusson, B.J.E., Letters, P.S., 2006b. The influence of weathering processes on riverine magnesium isotopes in a basaltic terrain. *Earth Planet. Sc. Lett.* 276, 187–197.
- Von Strandmann, P.A.E.P., Frings, P.J., Murphy, M.J., 2017. Lithium isotope behaviour during weathering in the Ganges Alluvial Plain. *Geochim. Cosmochim. Acta* 198, 17–31.
- Wei, X., Ji, H., Li, D., Zhang, F., Wang, S., 2013. Material source analysis and element geochemical research about two types of representative bauxite deposits and terra rossa in western Guangxi, southern China. *J. Geochem. Explor.* 133, 68–87.
- Whitehead, N.E., Hunt, J., Leslie, D., Rankin, P., 1993. The elemental content of Niue Island soils as an indicator of their origin. *New Zeal. J. Geol. Geop.* 36, 243–254.
- Wille, M., Babechuk, M.G., Kleinhans, I.C., Stegmaier, J., Suhr, N., Widdowson, M., Kamber, B.S., Schoenberg, R., 2018. Silicon and chromium stable isotopic systematics during basalt weathering and lateritisation: a comparison of variably weathered basalt profiles in the Deccan Traps, India. *Geoderma* 314, 190–204.
- Yaalon, D.H., 1997. Soils in the Mediterranean region: what makes them different? *Catena* 28, 157–169.
- Yalcin, M.G., Ilhan, S., 2008. Major and trace element geochemistry of Terra Rossa soil in the Kucukkoras region, Karaman, Turkey. *Geochem. Int.* 46, 1038–1054.
- Yang, J., Zhang, G., 2019. Si cycling and isotope fractionation: implications on weathering and soil formation processes in a typical subtropical area. *Geoderma* 337, 479–490.
- Young, G.M., Nesbitt, H.W., 1998. Processes controlling the distribution of Ti and Al in weathering profiles, siliciclastic sediments and sedimentary rocks. *J. Sediment. Res.* 68, 448–455.
- Zack, T., Tomascak, P.B., Rudnick, R.L., Dalpe, C., McDonough, W.F., 2003. Extremely light Li in orogenic eclogites: the role of isotope fractionation during dehydration in subducted oceanic crust. *Earth Planet. Sc. Lett.* 208, 279–290.
- Ziegler, K., Chadwick, O.A., Brzezinski, M.A., Kelly, E.F., 2005a. Natural variations of  $^{\delta 30}\text{Si}$  ratios during progressive basalt weathering, Hawaiian Islands. *Geochim. Cosmochim. Acta* 69, 4597–4610.
- Ziegler, K., Chadwick, O.A., White, A.F., Brzezinski, M.A., 2005b.  $^{\delta 30}\text{Si}$  systematics in a granitic saprolite, Puerto Rico. *Geology* 33, 817–820.